International Journal of Mining Science and Technology xxx (xxxx) xxx

Contents lists available at ScienceDirect

International Journal of Mining Science and Technology

journal homepage: www.elsevier.com/locate/ijmst

An experimental investigation into fluid injection-induced fault slip and fracturing under true triaxial stress

Linzhi Wang [a], Wu Cai [a,*], Wenzhuo Cao [b], Lee J. Hosking [c], Ruijia Wang [d], Mehdi Zare [e]

[a] State Key Laboratory for Fine Exploration and Intelligent Development of Coal Resources, China University of Mining and Technology, Xuzhou 221116, China
[b] Department of Earth Sciences, Utrecht University, Utrecht 3584 CS, the Netherlands
[c] Department of Civil and Environmental Engineering, Brunel University of London, London UB8 3PH, UK
[d] Department of Earth and Space Sciences, Southern University of Science and Technology, Shenzhen 518055, China
[e] Engineering Seismology Department, International Institute of Earthquake Engineering and Seismology, Tehran 19395/3913, Iran

ARTICLE INFO

Article history:
Received 31 December 2025
Received in revised form 17 March 2026
Accepted 19 May 2026
Available online xxxx

Keywords:
Fault slip
Fluid injection
Source mechanism
Spectral analysis
Acoustic emission monitoring

ABSTRACT

This study investigates fluid injection-induced fault slip under true triaxial stress, focusing on cases where injection boreholes are either hydraulically connected or disconnected from the fault. Through stress and displacement monitoring, acoustic emission analysis, spectral and source mechanism inversion, and CT scanning, three stages of fluid injection-induced fault slip were identified: injection-induced disturbance, hydraulic fracturing, and pore pressure buildup within the fault zone. The results reveal the dynamic evolution of fracture initiation, pressure accumulation, and fracture propagation leading to fault slip, and show that the fault slip state significantly influences pressure buildup. The observations confirmed a poroelastic coupling mechanism: as pore pressure within the fault zone rises, slip velocity initially increases with the injection rate and subsequently decreases. Source mechanism analysis indicates that fault slip is dominated by compressive-shear motion, whereas hydraulic fracturing exhibits tensile-shear characteristics. Rock mechanical strength, permeability, and stress field evolution analyses showed that fault reactivation precedes hydraulic fracturing of surrounding rock in hard rocks, whereas hydraulic fracturing occurs before fault slip in soft rock. In addition, for low-permeability faults, direct fluid injection is more effective in controlling slip than that for high-permeability faults.

1. Introduction

Seismic records provide essential insights into the release of tectonic stress associated with natural processes such as crustal deformation and plate motions, as well as for the impacts of activities including underground resource extraction, wastewater injection, and hydrological changes (Fig. 1). Industrial operations such as mining, oil and gas extraction, and geothermal energy production are increasingly recognised as key drivers of induced seismicity [1]. Seasonal climate changes, such as floods and droughts, have also been linked to seismic responses [2]. Globally, among over 1,000 recorded earthquakes, about 33% are associated with fluid injection and 25% with underground resource extraction [3]. These earthquakes span a wide range of magnitudes, from small earthquakes caused by local rupture of nearby rock to reactivation of major faults [4,5]. However, many induced earthquakes remain insufficiently studied. Specifically, in complex scenarios where hydraulic fractures propagate and intersect with adjacent faults, it remains to be clarified how high injection pressure drives the evolution of fracture networks and reconstructs seepage paths, thereby inducing fault instability. These critical hydro-mechanical coupling mechanisms require further elucidation.

Since Healy [6] first discovered that fluid injection can trigger fault slip and earthquakes, it has been widely accepted that injection-induced fault reactivation is governed by the Mohr-Coulomb fracture slip criterion and its extensions [7]. Two primary modes are recognised: (1) the pore pressure-dominated mechanism [8], which occurs when injected fluid directly enters the fault, raising pore pressure and reducing effective normal stress, and (2) the poroelastic coupling mechanism [9], in which injection-induced pressure alters the stress field, even when the injection well does not intersect the fault. In the latter case, stress perturbations can extend over long distances, reaching up to 10 km [10].

There is a growing consensus that fluid injection can induce acoustic emission (AE) activity in the laboratory corresponding to microseismic events at field scale, serving as an indicator of fault reactivation. Researchers typically employ three methods, i.e., sta-

* Corresponding author.
E-mail address: caiwu@cumt.edu.cn (W. Cai).

https://doi.org/10.1016/j.ijmst.2026.05.006
2095-2686/

Please cite this article as: L. Wang, W. Cai, W. Cao et al., An experimental investigation into fluid injection-induced fault slip and fracturing under true triaxial stress, International Journal of Mining Science and Technology, https://doi.org/10.1016/j.ijmst.2026.05.006

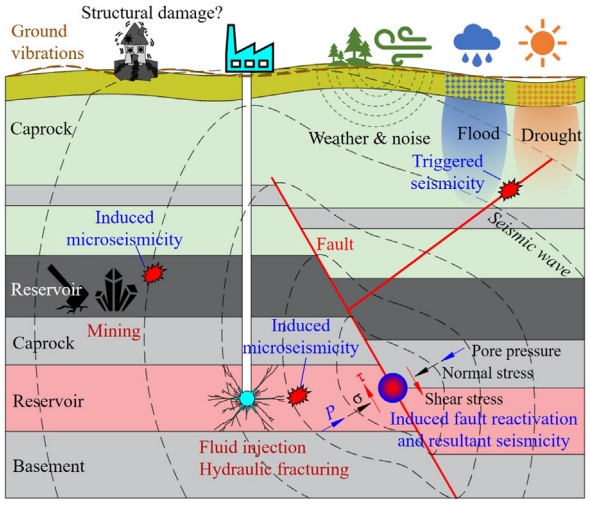

Fig. 1. Schematic diagram of mechanisms for fault reactivation and induced seismicity.

tistical analysis, source parameter solution, and physical mechanism analysis, to assess seismic risks associated with fluid injection [11]. The statistical method primarily relies on microseismic catalogues to calculate changes in statistical characteristics of micro seismicity, and compare them with background levels of historical seismicity, thereby clarifying the relationship between induced earthquakes and fluid injection activities [12]. In recent years, probabilistic optimisation statistical models, developed based on the Random sample consensus (RANSAC) random sampling consistency method, have been widely applied to reconstruct discrete fracture networks [13].

Source parameters primarily examine the microseismic characteristics of fluid injection-induced fault reactivation by establishing correlations between the spatiotemporal attributes of microearthquakes and fault conditions or fluid injection parameters. For example, spatiotemporal microseismic parameters have been linked to variations in fluid injection parameters [14]. Additionally, the spatiotemporal distribution patterns of fluid injection-induced micro seismicity have been analysed through clustering techniques [15]. Moment tensor inversion enables the differentiation between signals associated with hydraulic fracturing and those stemming from fault slip [16], and can also support the reconstruction of discrete fracture networks [17].

Physical mechanism analysis integrates laboratory experiments, field measurements, and numerical simulations to examine the microseismic and AE response associated with fluid injection-induced fault reactivation. Multiphysics numerical models have been used to simulate fluid injection-induced fault reactivation processes and their seismic response [18]. This approach also provides insights into the spatiotemporal distribution of induced seismicity [19] and its correlation with fluid injection pressure and temperature [20]. Additionally, a random discrete seismic activity model has been introduced to simulate microseismic catalogues and validate them against field monitoring data [21]. Furthermore, laboratory experiments [22] and field studies [23] have been employed to analyse the spatiotemporal characteristics and spectral signatures of microseismic and AE events associated with fluid injection-induced fault reactivation.

Controlled laboratory experiments have systematically examined the influencing factors and coupled processes of fluid injection-induced fault reactivation, using small-scale prefabricated samples [24], large-scale prefabricated fault blocks [25], and even near field-scale fluid injection experiments into faults [26]. The findings indicated that fluid injection-induced fault reactivation is a dynamic process influenced by parameters such as injection rate, pore pressure evolution, fault permeability, and frictional properties. This process comprises two stages: fault reactivation and subsequent fault slip. The latter may occur in two regimes: stable slip (constant velocity or velocity decay) and unstable slip (velocity acceleration) [27]. During the reactivation stage, high injection rates can cause rapid pore pressure buildup on the fault, promoting fault slippage or dynamic rupture [28]. In contrast, low injection rates promote fault activation primarily through a progressive reduction in effective normal stress on the fault [29]. During the slip stage, pore pressure is the key physical variable that controls the transition from stable to unstable slip. The injection rate and fault permeability jointly govern pore pressure evolution: increased permeability promotes the dissipation of pore pressure, while high injection rates dominate the accumulation of pore pressure. Their interaction determines whether fault slip is stable or unstable. Studies have shown that fault permeability and slip rate increase nonlinearly during slip [30], reflecting the complex feedback between fluid flow, effective stress, and slip behaviour.

Currently, laboratory fluid-solid coupling experiments predominantly utilise small-scale prefabricated cylindrical specimens [31]. However, these specimens face limitations in capturing the influence of fluid injection-induced fracturing on fault reactivation under true triaxial stress [32], as well as the localised fracturing processes that occur within the fault zone. Furthermore, experimental schemes that systematically incorporate multiple interacting factors remain challenging, making it difficult to develop models that realistically represent in-situ geological conditions. Many existing studies focus narrowly on the hydraulic fracture propagation in intact rock masses [18,19] or on fluid injection-induced fault reactivation mechanisms [33], without adequately addressing their combined effects. Therefore, conducting true triaxial fluid injection and fracturing experiments using large-scale faulted rock specimens enables comprehensive investigation of complex stress environments, multi-factor interactions, and fluid migration behaviour.

This study is situated within the engineering context of underground mineral resource exploitation and geothermal resource development. It examines the fluid injection-induced fault reactivation mechanisms and the associated seismic response under conditions where injection boreholes are either hydraulically connected to, or isolated from, the fault.

2. Experimental design and procedure

2.1. Experimental design

The 150 mm cubic blocks were diagonally cut into two symmetric halves. Following rough and fine grinding of the interfaces, the halves were reassembled in direct contact.

The experimental samples comprise yellow sandstone obtained from a surface quarry in a specific mining area in Xuzhou, China. The samples are characterised by a distinct sedimentary stratified structure. Cubic samples of 150 mm in each dimension diagonally cut into two symmetric halves. Following rough and fine grinding of the interfaces, the halves were reassembled in direct contact. The measured friction coefficient of the sandstone is 0.33. The samples were categorised into two groups: one with a fluid injection drillhole connected to the fault plane, and one with a drillhole disconnected from the fault plane, with three samples in each group. For the connected group, an 80 mm long, 10 mm diameter drillhole was prefabricated at the midpoint of the top surface. In the disconnected group, a 50 mm long, 10 mm diameter drillhole was created at the centre of the top surface. The fault plane in all samples was inclined at 45° (Fig. 2).

Fig. 3 presents result of preliminary basic parameter characterisation. The samples, measuring 50 mm × 50 mm × 100 mm, were subjected to a loading rate of 0.1 MPa/s under confining pressures of σ_3=5 MPa and σ_2=6 MPa, while the fluid injection pressure was maintained at 4 MPa. Specifically, Fig. 3a depicts results of triaxial seepage experiments, and Fig. 3b illustrates results of triaxial loading experiments. The magnitude of the permeability (k) is around 10^{-17} m^2, showing the low-permeability of the samples.

The experimental setup employs a PWS-1500 true triaxial stress loading system to establish a stable true triaxial stress environment. To maintain constant flow injection, an LC-3060B micro constant pressure and constant flow dual-mode booster pump was utilised. AE monitoring and analysis were conducted using a Milne AE signal monitoring system and the InSite-Lab data processing system (Itasca Consulting Group, UK), as illustrated in Fig. 4.

2.2. Experimental procedure

2.2.1. Stress loading path

The Mohr-Coulomb failure criterion is commonly used to evaluate fault reactivation [34]:

$$\tau \geqslant \tau_{\text{crit}} = \mu \cdot (\sigma_n - p) + c_f \tag{1}$$

where τ_{crit} is the critical shear stress for fault activation; τ and σ_n the fault shear stress and normal stresses, respectively; μ the fault friction coefficient; p the pore pressure; and c_f the fault cohesion (zero in this experiment).

For specimens with a fault inclination angle of 45°, σ_n and τ on the fault are given by:

$$\sigma_n = \frac{\sigma_1 + \sigma_3}{2} \tag{2}$$

$$\tau = \frac{\sigma_1 - \sigma_3}{2} \tag{3}$$

Using the friction coefficient measured as 0.33 in the preliminary tests, the fault reaches a critical state when Eq. (1) is satisfied. Using Eqs. (2) and (3), the following conditions must therefore be satisfied:

$$\frac{\sigma_1 - \sigma_3}{\sigma_1 + \sigma_3 - 2p} = 0.33 \tag{4}$$

Disconnected samples: Stress is applied simultaneously in the σ_1, σ_2, and σ_3 directions at a loading rate of 0.1 MPa/s. The stresses are held constant once σ_3=5 MPa, σ_2=6 MPa, and σ_1=10 MPa. After stabilisation, fluid injection is applied at 10 mL/min from 132 to 567 s, 20 mL/min from 568 to 629 s, and 49 mL/min from 630 s until the end of the experiment.

Connected samples: Stress is applied simultaneously in the σ_1, σ_2, and σ_3 directions at a loading rate of 0.1 MPa/s. The stresses are held sequentially when σ_3=10 MPa, σ_2=12 MPa, and σ_1=20 MPa. Following the stabilization of the triaxial stress at 246 s, hydraulic fracturing is conducted at a constant flow rate of 49.99 mL/min.

2.2.2. Monitoring plan

The experimental system's acquisition instruments are used to collect stress and displacement data continuously. Fluid injection volume and pressure are monitored in real time through the flow control and pressure sensors. AE signals are recorded using probes mounted on the loading head. Four probes are arranged on each loading surface in a "+" configuration to monitor signals from fault slip and micro-fracturing. AE signals are sampled at 10 MHz. To minimize the frictional interference from the loading platens, a uniform layer of Vaseline was applied to the specimen surfaces during the experimental preparation phase.

To intuitively illustrate the derivation of the fault slip, a geometric schematic is presented in Fig. 5. The net fault slip vector ΔL along the fault plane is determined by the geometric projection of the vertical displacement (Δy) at the top boundary and the horizontal displacements (Δx_1, Δx_2) at the lateral boundaries. Consequently, the fault slip can be calculated using the following [22]:

$$\Delta L = (\Delta y + \Delta x)/2 \cos\theta \tag{5}$$

where Δx=Δx_1−Δx_2. θ is the inclination angle of the fault.

3. Results

3.1. Fluid injection pressure

Fig. 6 illustrates the fluid injection process for the hydraulically disconnected sample group, with Fig. 5b showing key behaviour

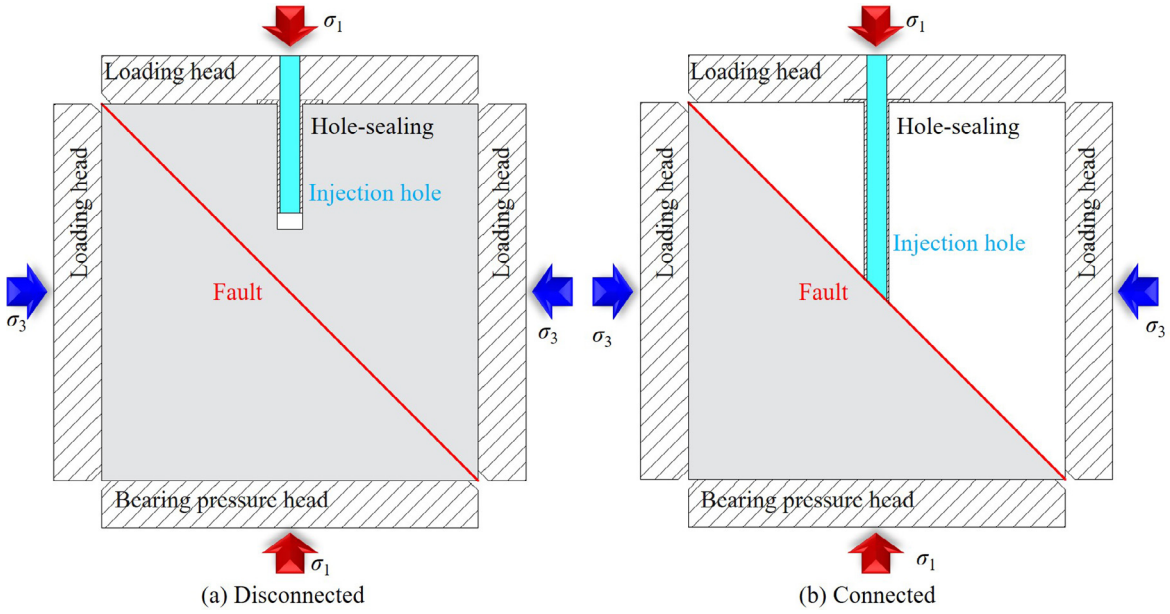

Fig. 2. Prefabricated fault-containing cubic samples prepared for laboratory fluid injection experiments under true triaxial stress.

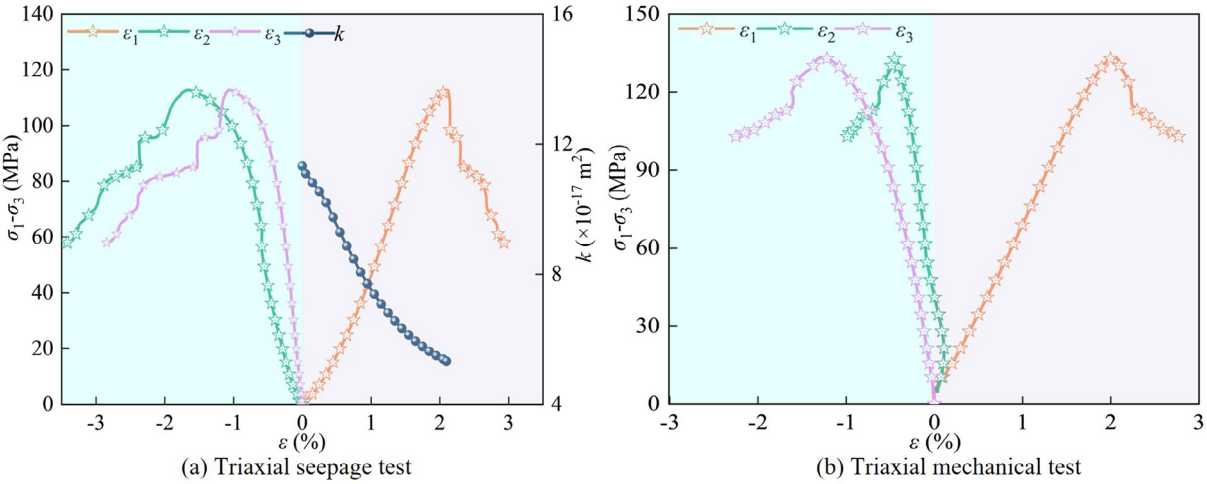

Fig. 3. Basic mechanical parameter characterisation of the sandstone samples.

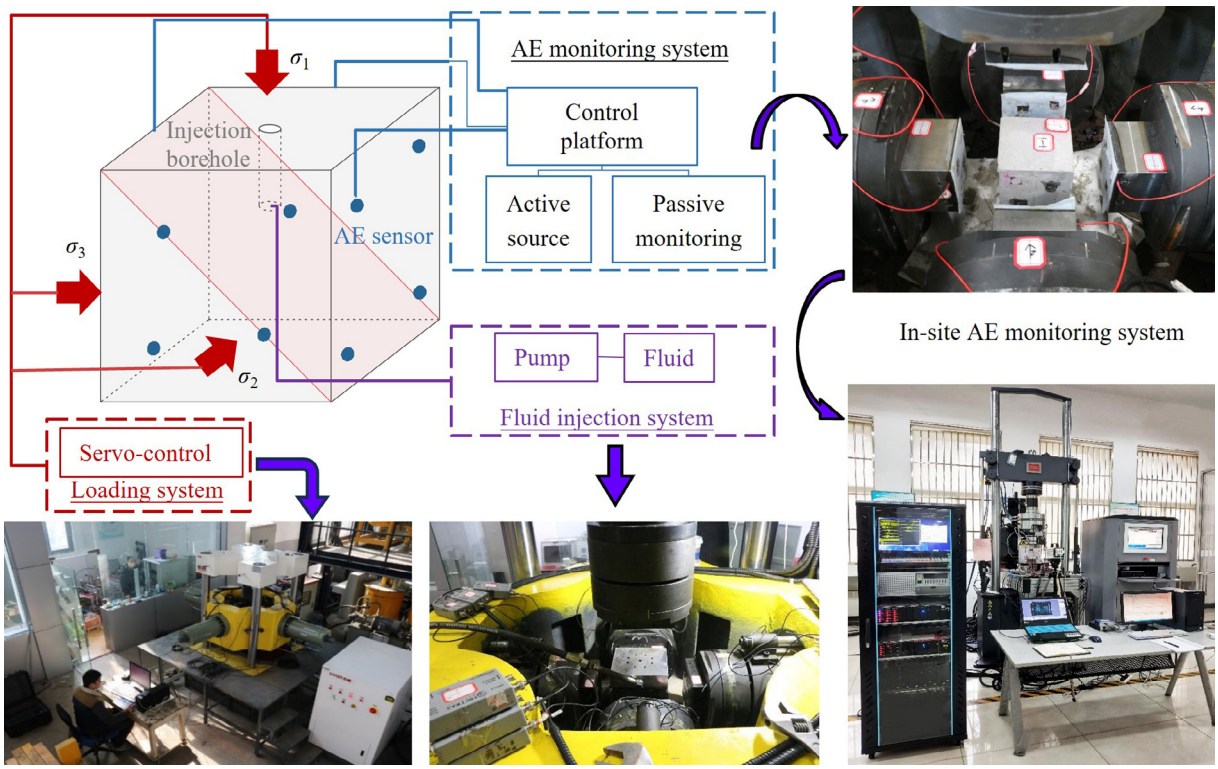

Fig. 4. True triaxial fluid injection-induced fault slip and fracturing experimental setup, equipped with AE monitoring and analysis systems.

exhibited in five stages: the fluid injection disturbance stage (132–237 s), the hydraulic fracturing stage (238–370 s), the connection of fractures and fault stages at injection rates of 10 mL/min (371–567 s), 20 mL/min (568–629 s), and 50 mL/min (630 s). Throughout the fluid injection fracturing stage, the injection pressure exhibits a characteristic pattern of increasing, decreasing, and increasing again. The injection pressure peaks reach to 7 MPa at 147 s, 10.8 MPa at 237 s, 11.2 MPa at 259 s, 12.1 MPa at 280 s, and 11.9 MPa at 372 s. This process indicates that fracture propagation during hydraulic fracturing is not instantaneous but instead involves a dynamic sequence of sample rupture, fracture compression, and fracture extension.

A remarkable gap is evident between the initial pressure peak and the subsequent peaks, with later peaks remaining at a relatively stable level. This difference arises from stress concentration and initial damage occurring near the fluid injection orifices at the base of the sample, which reduced the local rupture pressure relative to the intact rock. During the fluid injection disturbance phase, before water has penetrated the fault, stress distribution is predominantly influenced by poroelastic stress [10], resulting in a nonlinear fault slip curve.

Due to the direct connection between the water injection hole of the specimen with connectivity and the fault, water directly influences the pore water pressure at the fault, thereby altering its slip state. This process occurs without disturbance from poroelastic stress effects (Fig. 7). Under conditions of constant confining pressure and water injection rate, the pore pressure at the fault exhibits minor fluctuations, as shown in Fig. 7b: for instance, the

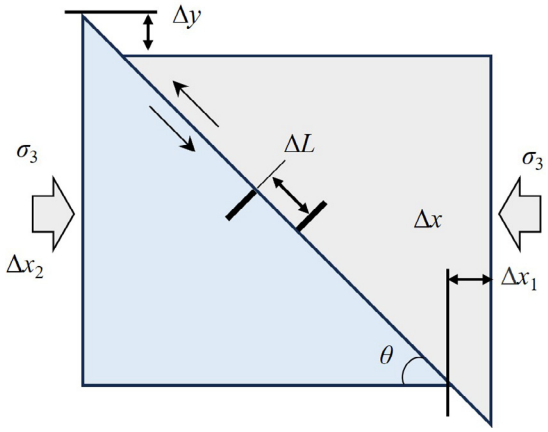

Fig. 5. Geometric schematic illustrating the calculation of the fault slip vector.

injection pressure decreases from 5 MPa at 573 s to 4.5 MPa at 576 s, then gradually recovers to 5 MPa. According to Darcy's law, the pore water pressure at the fault decreases linearly, which increases the non-uniformity of stress distribution along the fault. Consequently, while promoting overall fault slip, localized failure also occurs within the fault, leading to minor fluctuations in the injection pressure.

3.2. Spatio-temporal distribution of AE events

The AE events are plotted in a two-dimensional time-lapse view, enabling the visualisation of the failure sequence within the rock and the evolution of the fault reactivation throughout the injection process. As demonstrated in Fig. 8a, during the stress adjustment phase of the hydraulically disconnected sample group, AE events initially clustered along the fracture layer before shifting toward the base of the fluid injection hole. This observation implies that the base of the injection hole exhibits inherent structural weakness during sample preparation, an effect that may also occur in field applications, resulting in AE events at that location.

During the fluid injection stage of the hydraulically disconnected sample (Fig. 8b), AE events occur along the fault early in the injection process. By 13 s after injection starts, AE events are already observed at the fault, even though fluid has not yet seeped into it. This observation indicates that the poroelastic stress near the injection hole activates the fault, demonstrating that the poroelastic coupling is the dominant mechanism driving fault reactivation during fluid injection.

Fig. 9 presents the spatio-temporal distribution of AE events in the hydraulically connected samples throughout the experiment. In the stress adjustment phase (Fig. 9a), AE events are more broadly distributed compared to those observed during the fluid injection phase (Fig. 9b). This difference arises from the elevated pore fluid pressure at the base of the injection hole, located on the fault, during fluid injection, leading to a linear pressure reduction in this region. Consequently, stress rapidly redistributes in this region, resulting in a concentration of AE events. A clear contrast in AE event frequency between the hydraulically connected and disconnected samples is evident when comparing Figs. 8b and 9b. The frequency of AE events is markedly lower in the disconnected samples than in connected ones. By classifying the associated fault slip behaviour, it becomes apparent that the lateral slip in disconnected samples corresponds to aseismic slip [35], while the slip in connected samples corresponds to seismic slip.

Following the experiment, industrial CT scans were performed on the disconnected samples after hydraulic fracturing. The scanning parameters were set to a voltage of 440 kV, a current of 1.5 mA, an exposure time of 0.45 s, and a scanning duration of 1 h. This process yielded a three-dimensional reconstruction of the internal fractures within the samples, with a resolution of 90.2 μm, as illustrated in Fig. 10.

In Fig. 10, the brown areas represent the pore pressure monitoring holes and the damaged regions at the base of these holes formed during loading. The green regions indicate the damaged areas at the intersection between the hydraulic fracturing holes and the pore pressure monitoring holes. The cyan regions denote the pore pressure monitoring holes. During the experiment, shear misalignment between the loading fixture and the sample caused the connection wire of the pore pressure sensor to break, resulting in the loss of monitoring data. This sensor was intended to capture the pore pressure evolution following the fluid injection conduction section, thereby indirectly characterising the permeation process and the fracture propagation path. Due to the absence of data, CT scanning was used subsequently to complement and verify the observations. Furthermore, this method effectively validates the accuracy of AE event localisation.

The blue regions indicate the hydraulic fracturing holes and the zones where fractures form during the fracturing process. Fractures initially extend from the injection hole towards the fault plane. This extension is driven by stress concentration at the base of the injection hole during the stress adjustment phase, which facilitates the formation of early fractures. During the early fluid injection stage, fluid travels along these initial fractures, which stimulates their further development and coalescence into larger fractures. A similar phenomenon is observed in the hydraulically connected samples (Fig. 10c): once fractures reach into a critical extent, they propagate preferentially in the direction of the minimum principal stress, σ_{xy}, which is perpendicular to the fault. Ultimately, the fractures reach the fault, establishing a hydraulic connection between the injection hole and the fault.

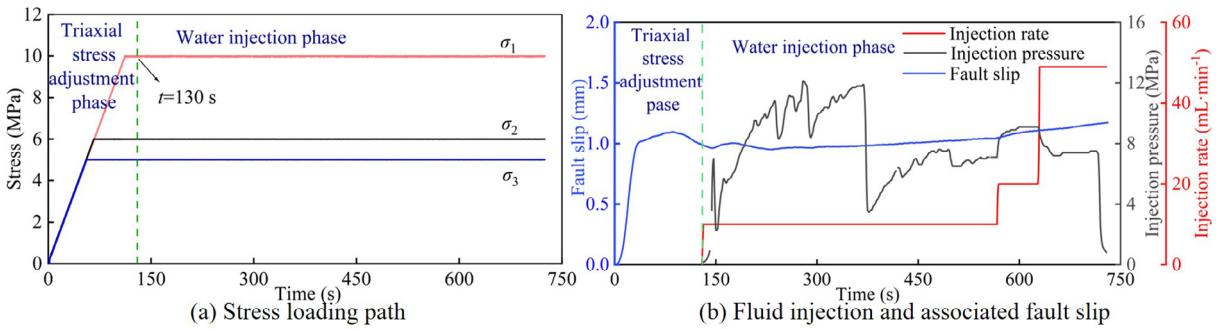

Fig. 6. Experimental procedure and results for the hydraulically disconnected specimen.

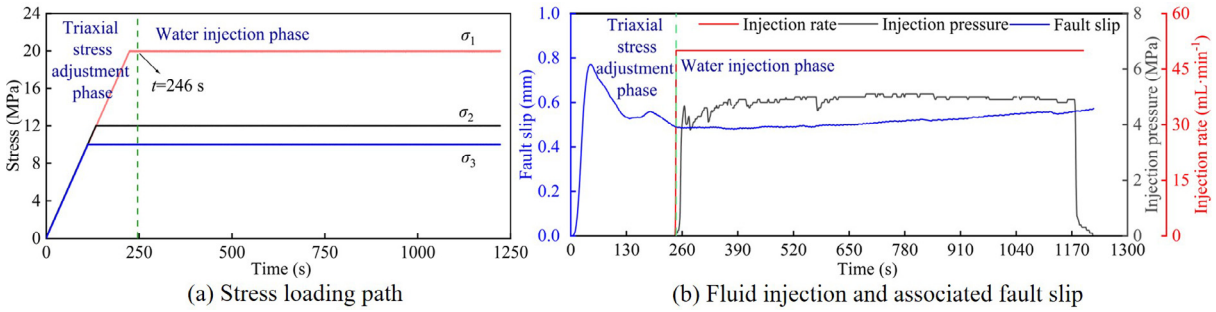

(a) Stress loading path (b) Fluid injection and associated fault slip

Fig. 7. Experimental procedure and results for the hydraulically connected sample group.

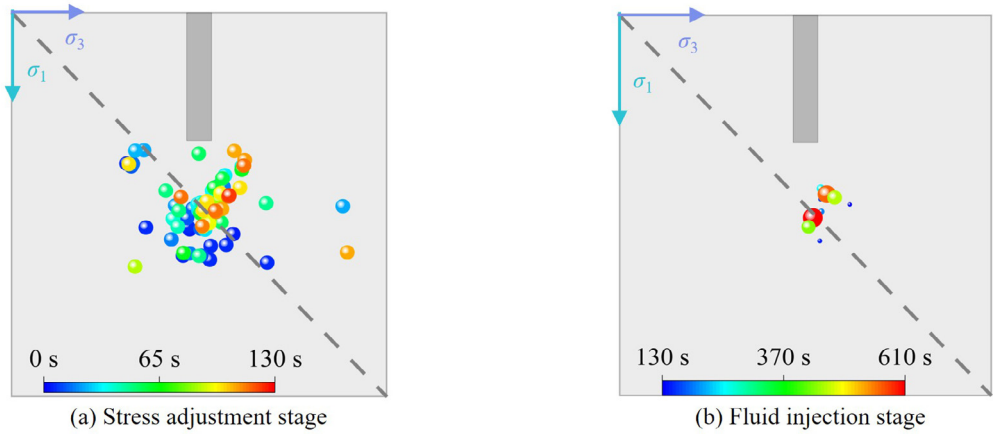

(a) Stress adjustment stage (b) Fluid injection stage

Fig. 8. Spatio-temporal distribution of AE events in hydraulically disconnected samples.

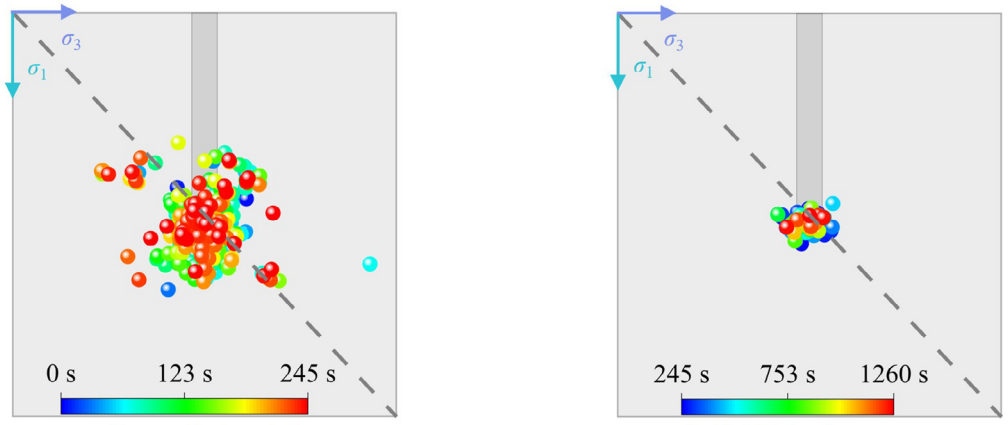

(a) Stress adjustment stage (b) Fluid injection stage

Fig. 9. Spatio-temporal distribution of AE events in hydraulically connected samples.

3.3. AE event types and sequences

During the fluid injection period for the hydraulically disconnected samples, a total of 13 events were recorded (Fig. 8b). These included 6 events during the injection disturbance stage, 1 event during the fracturing stage, 4 events in the first injection stage, 2 events in the second injection stage, and none in the third injection stage. Fig. 11 presents the short-time Fourier transform, using a unified channel to capture the waveform, duration, frequency, and energy distribution of each AE event. According to reference [23], AE events can be classified into three main categories: seismic events (SE), long-period events (LP), and tremor-like signals (TLS).

A comparison of AE signals observed in volcanoes [36], reservoirs [37], and landslides [38] reveals that the SE-type signals correspond to typical fault slip behaviour. The narrow frequency band of LP-type signals primarily arises from a decrease in fluid pressure caused by cavity resonance, which occurs when fractures or voids are filled with fluid. In contrast, the prolonged duration and distinctive waveform characteristics of TLS-type signals imply that the fault is experiencing slow slip.

Fig. 11 illustrates evolution of AE activity during the fluid injection process. At the onset of injection (139 s), an LP event signal indicates the initial entry of fluid into the fracture, where pressure begins to accumulate. Subsequently, as the pressure increases,

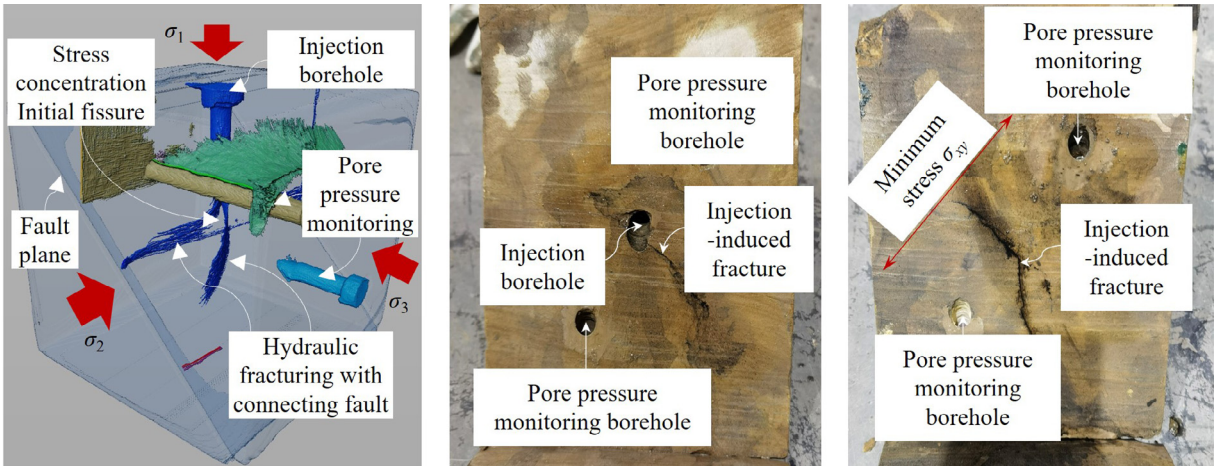

Fig. 10. Fracture propagation paths during hydraulic fracturing.

poroelastic stress perturbations induce fault slip and generate SE events (143 s, 148 s). This slip relieves local pressure, causing a drop in injection pressure and resulting in a TLS event (150 s). Continuous injection elevates pore pressure, which promotes fracture growth and produces additional LP events (253 s). Once a hydraulic connection is established between the injection hole and the fault, AE events are dominated by SE signals. Increasing the injection rate from 10 mL/min to 20 mL/min further enhances fault reactivation, leading to additional SE events (599 s, 610 s). It is worth noting that the signal at 599 s exhibits transitional characteristics between SE and TLS events. We attribute this to the increased injection rate, which not only induces further hydraulic fracture propagation but also alters the fault slip state. In this study, the classification is primarily based on the duration of the dominant frequency band. For instance, the event at 150 s is classified as a TLS due to its sustained broadband energy over a long duration. In contrast, although the 599 s event exhibits a coda, the duration of its high-energy frequency band is relatively short compared to typical TLS events, warranting its classification as an SE.

For the hydraulically connected sample, a total of 319 valid AE events is generated during the fluid injection stage. Here, 10 representative AE events from different stages were selected for analysis (Fig. 12), including the initial injection stage, the stage with significant pressure fluctuations (562–601 s), and the stage of relatively stable pressure. Fig. 12 illustrates that the AE events in the hydraulically connected sample primarily consist of SE events, with LP events occurring at 265, 266, and 574 s. These AE events consistently coincide with moments of fluid injection pressure fluctuations.

Additionally, Figs. 11 and 12 illustrate that fault reactivation induced by hydraulic fracturing is not a simple process whereby hydraulic pressure drives the fractures toward and into the fault. Instead, this process involves a dynamic feedback loop: fluid injection promotes fracture propagation, fault slip locally relieves pressure, and such pressure redistribution subsequently facilitates further fracture development. Furthermore, the evolution of AE event type provides an effective and timely indicator of instability within the surrounding rock during the injection-induced fault slip.

3.4. Seismic response to hydraulic fracturing and fault slip

3.4.1. Fundamentals of moment tensor inversion

The moment tensor inversion method calculates the equivalent stress associated with a seismic source by utilising the internal displacement of the rock mass recorded during rupture, together with the pulse function (Green's function) that characterises the medium's response [39]. Assuming that the source dimension is significantly smaller than the observation distance and the dominant seismic wavelength, the source can be treated as a point source. The moment tensor M represents the force system acting at the source. Under the assumption of a synchronous source, the displacement amplitude recorded at monitoring station i can be expressed as:

$$u_i(x,t) = M_{jk} G_{i,jk}(x, x_0, t) \tag{6}$$

where $G_{i,jk}$ is the Green's function representing the impulse response of the medium between the source location x_0 and the monitoring point x; and M_{jk} moment tensor component, with subscripts j and k denoting the position and direction of the applied forces. The moment tensor M in the Cartesian coordinate system is defined by Eq. (7).

$$M = \begin{bmatrix} M_{11} & M_{12} & M_{13} \\ M_{21} & M_{22} & M_{23} \\ M_{31} & M_{32} & M_{33} \end{bmatrix} \tag{7}$$

The moment tensor M can be decomposed into three components: the double-couple (DC), the compensated linear vector dipole (CLVD), and the isotropic part (ISO) through the eigenvalue decomposition method, as expressed by:

$$M = M^{\mathrm{ISO}} + M^{\mathrm{CLVD}} + M^{\mathrm{DC}} \tag{8}$$

where,

$$M^{\mathrm{ISO}} = \frac{1}{3}\mathrm{tr}(M)\begin{bmatrix} 1 & 0 & 0 \\ 0 & 1 & 0 \\ 0 & 0 & 1 \end{bmatrix},\ M^{\mathrm{CLVD}} = |\varepsilon| M^{*}_{|\max|}\begin{bmatrix} -1 & 0 & 0 \\ 0 & -1 & 0 \\ 0 & 0 & 2 \end{bmatrix},$$

$$M^{\mathrm{DC}} = (1 - 2|\varepsilon|) M^{*}_{|\max|}\begin{bmatrix} -1 & 0 & 0 \\ 0 & 0 & 0 \\ 0 & 0 & 1 \end{bmatrix}$$

The sum of the ISO and CLVD components is referred to as the non-DC component, while CLVD and DC components together constitute the moment tensor part M^{*}. The parameter ε represents the magnitude of CLVD with respect to the DC component and is defined as:

$$\varepsilon = -\frac{M^{*}_{|\min|}}{\left|M^{*}_{|\max|}\right|} \tag{9}$$

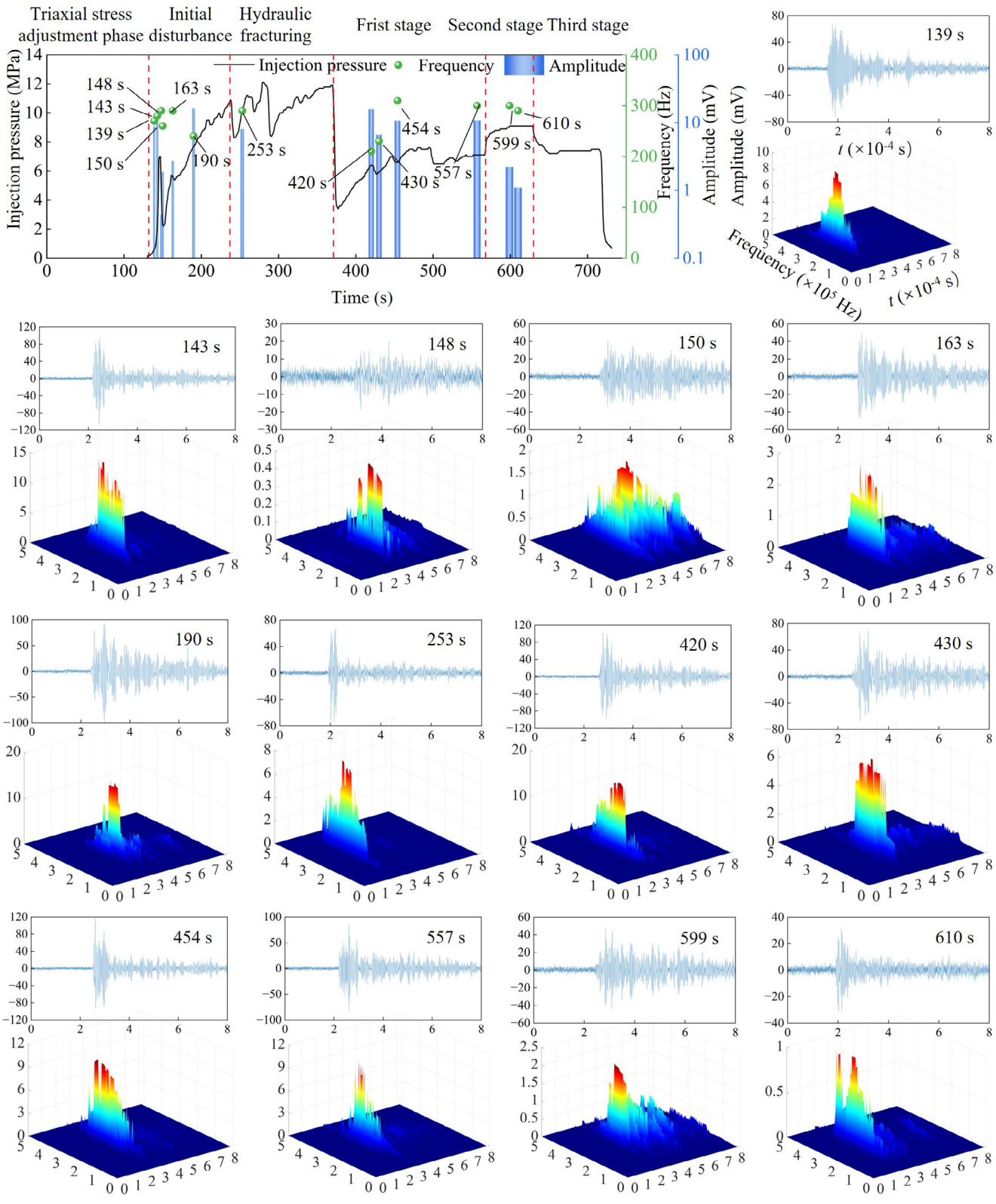

Fig. 11. Time-frequency analysis of AE events during fluid injection into hydraulically disconnected samples.

where $M^*_{|max|}$ and $M^*_{|min|}$ are the maximum and minimum absolute values of the eigenvalues of M^*, respectively.

The source mechanism of AE events generated in the experiments with hydraulically connected and disconnected samples was determined using the aforementioned method. A reliability test was conducted based on the T-K value error of the moment tensor [31], where smaller values indicate more reliable inversion results. The statistical outcomes are presented in Fig. 13, showing

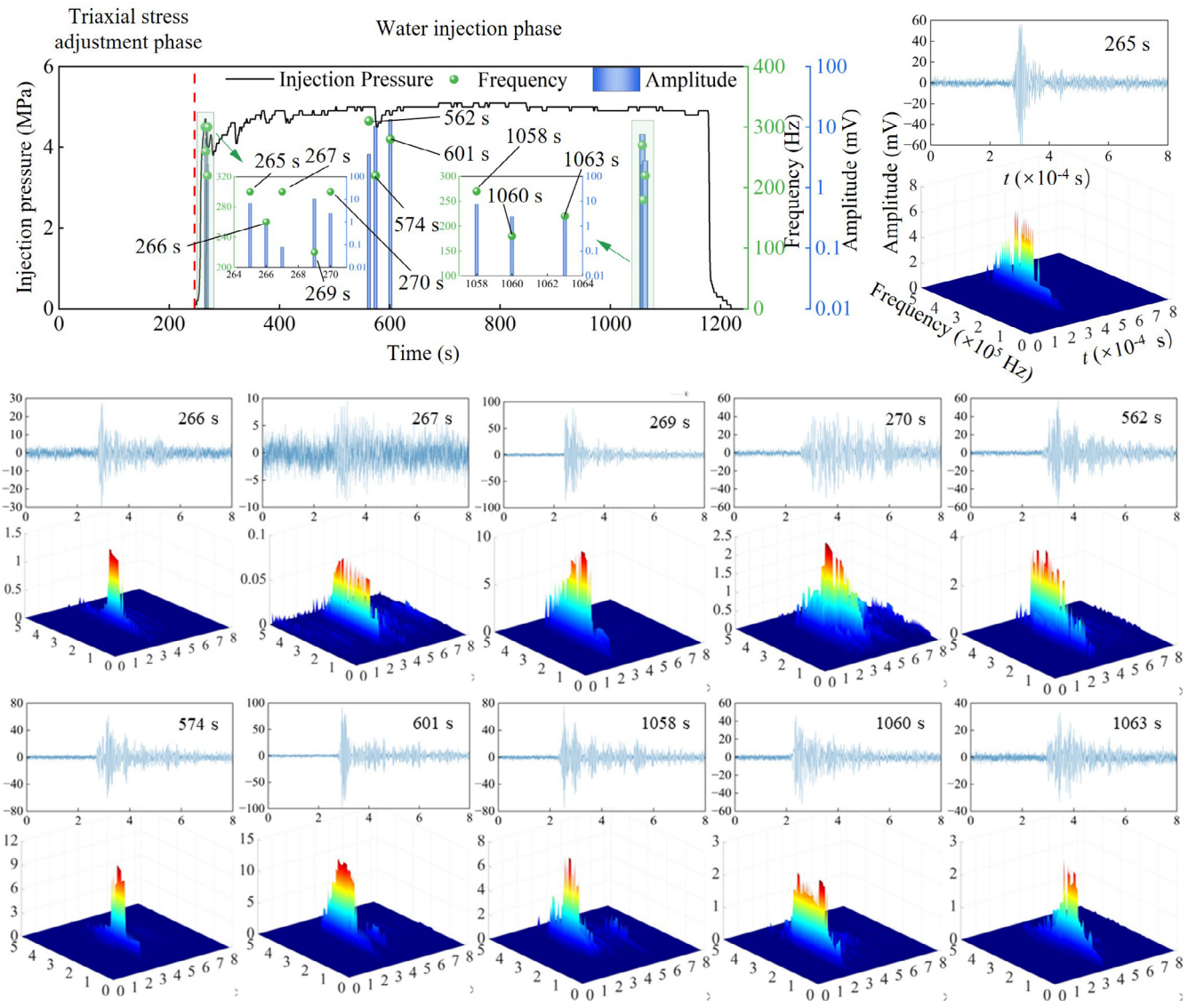

Fig. 12. Time-frequency analysis of AE events during fluid injection into hydraulically connected samples.

that 76% of the calculated results exhibit test values below 10, thereby confirming the reliability of the seismic source mechanism solutions obtained in this experiment.

Hudson [40] performs specific transformations on the three eigenvalues of the moment tensor, m_1, m_2, and m_3 (m_1>m_2>m_3), to characterise the source type. By considering the sign of the intermediate eigenvalue m'_2 in DEV, the tensile component k and the shear component T can be calculated:

$$(k,T)=\begin{cases}\left(\frac{M_{ISO}}{|M_{ISO}|-m'_3},\frac{-2m'_2}{m'_3}\right)m'_2>0\\ \left(\frac{M_{ISO}}{|M_{ISO}|+m'_1},0\right)m'_2=0\\ \left(\frac{M_{ISO}}{|M_{ISO}|+m'_1},\frac{-2m'_2}{m'_1}\right)m'_2<0\end{cases}\quad(10)$$

where the eigenvalue of DEV is $m'_2 = m_i$-M_{ISO}, and DEV satisfies tr $(M_{DEV}) = m'_1 + m'_2 + m'_3$.

3.4.2. Seismic characteristics of fluid injection-induced fault slip

Fig. 14 presents the T-K distribution of the AE event source mechanisms for the hydraulically disconnected sample during the stress adjustment stage and the hydraulic fracturing stage, alongside selected source mechanism solutions. As indicated in

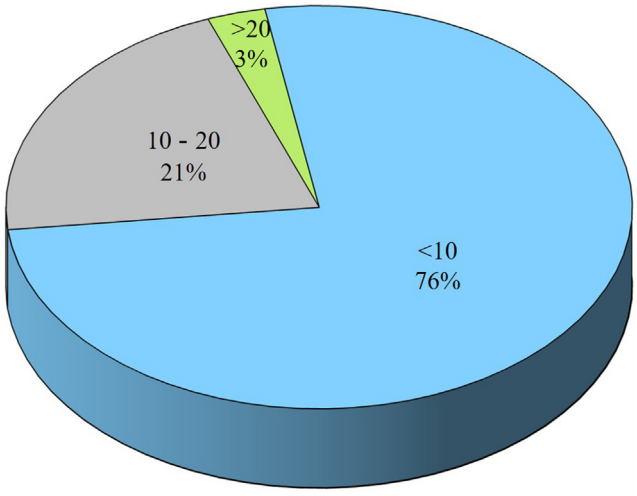

Fig. 13. Test value statistics for source mechanism solutions.

Fig. 8b, the failure type near the bottom of the injection hole is dominated by tensile-shear behaviour, whereas the failure mode near the fault primarily demonstrates compressive-shear characteristics. Fig. 15 illustrates the T-K distribution of the AE event source mechanisms for the hydraulically connected sample during the same stages, along with representative source mechanism results. The findings reveal a similarity to those observed in the hydraulically disconnected sample.

Fig. 16 illustrates the proportions of seismic source mechanisms for the different samples at each stage. Here, DSA denotes the stress adjustment stage for the disconnected sample, DWI the water injection stage for the disconnected sample, CSA the stress adjustment stage for the connected sample, and CWI the fluid injection stage for the connected sample.

Across all conditions, the dominant failure modes are compressive-shear and tensile-shear. The tensile-shear failures primarily stem from stress concentration at the base of the injection hole, while the compressive-shear failures result from the combined effects of fault shear stress and normal compressive stress during slip. In the later phase of fluid injection, for the disconnected sample, failures near both the injection hole base and the fault, compression-shear types for the highest proportion. Analysis of seismic source types during fluid injection reveals a decrease in the proportions of compression-shear and tensile-shear events by 3.9% and 3.8%, respectively. In contrast, shear and other types (e.g., implosion events) have increased by 3.2% and 4.5%, respectively. These results suggest that fluid injection does not change the overall dominance of compression-shear and tensile-shear failures when the fault is unstable. Nonetheless, the increase in pore pressure induced by fluid injection heightens the local heterogeneity in the stress distribution near the injection hole, leading to additional non-shear seismic events.

3.5. Correlation between fluid injection rate and fault slip

Given that both hydraulically connected and disconnected samples undergo triaxial deformation during stress loading, the following analysis focuses solely on fault slip during the fluid injection phase to limit strain-related interference. Fig. 17 illustrates linear fits of fault slip displacement under different fluid injection rates.

As illustrated in Fig. 18, the process of fault activation induced by fluid injection can be primarily categorized into two distinct stages:

(1) Slip acceleration stage (Stage A to B): As the injection rate increases (from point A to point B3), the fluid permeates the fault zone, increasing the water pressure gradient. This induces an increase in strain heterogeneity, which, at this stage, primarily lubricates the fault and leads to a decrease in the friction coefficient. In the Mohr circle diagram

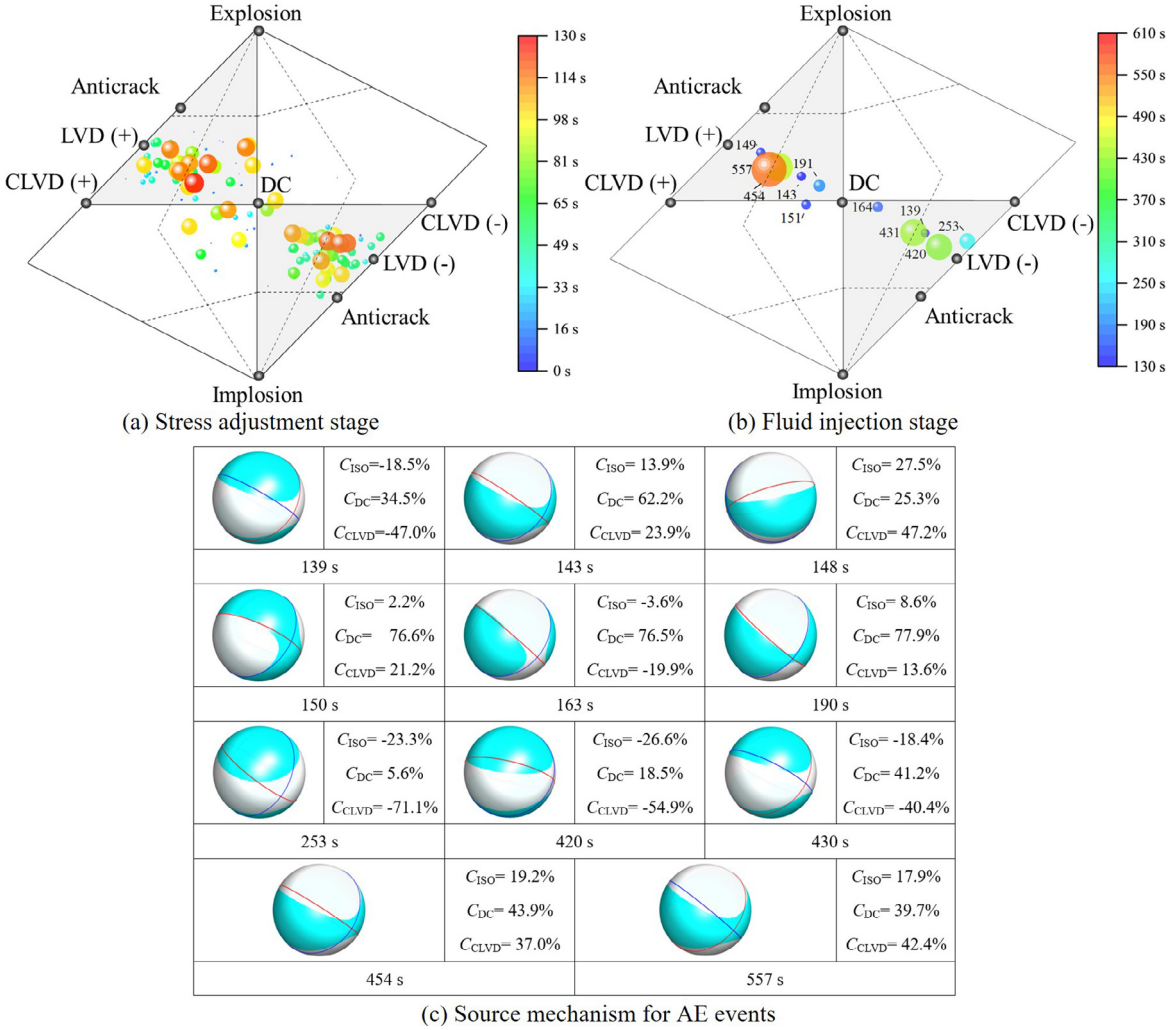

Fig. 14. Source mechanisms for AE events at different stages of the hydraulically disconnected sample.

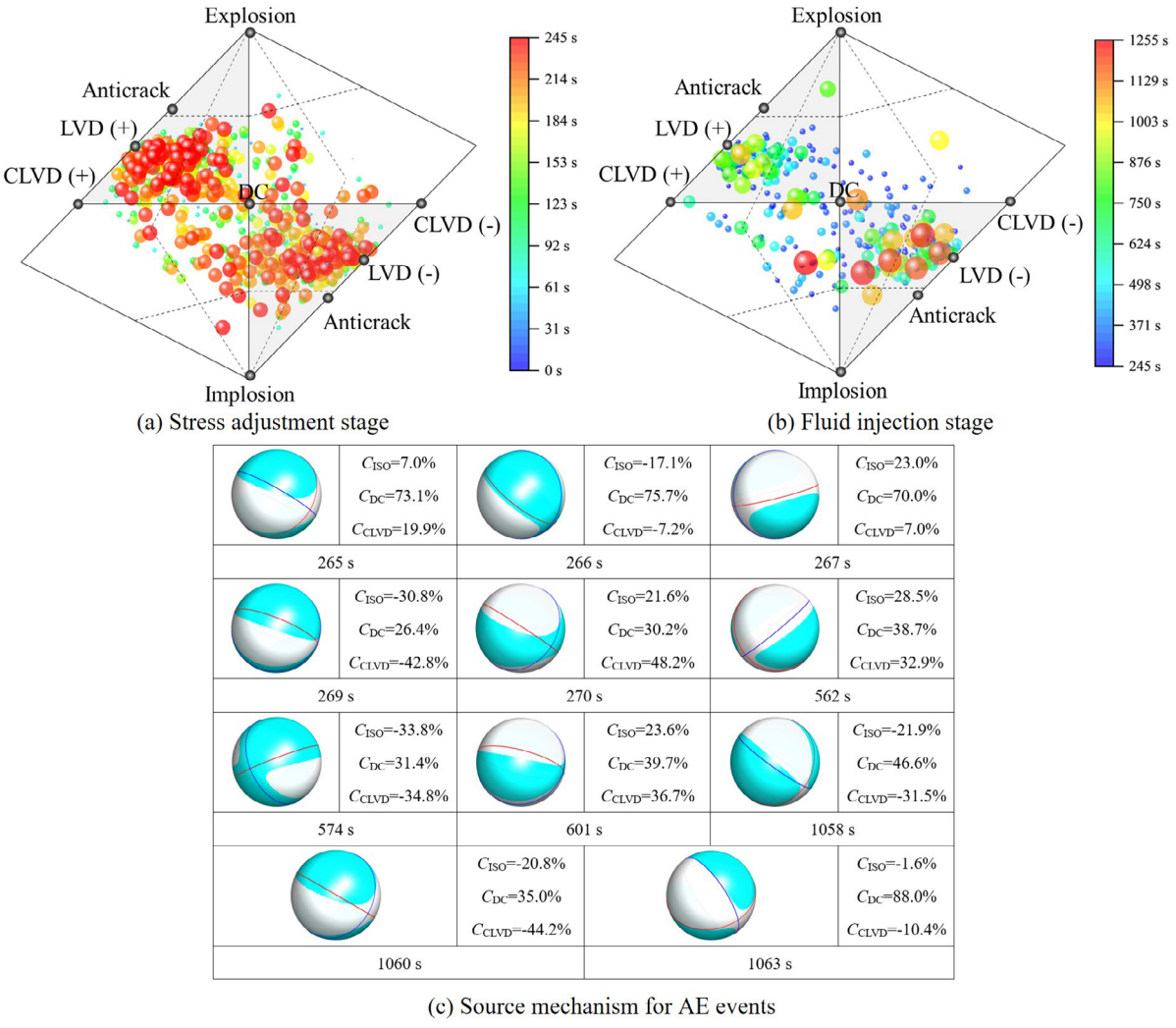

Fig. 15. Source mechanisms for AE events at different stages of the hydraulically connected sample.

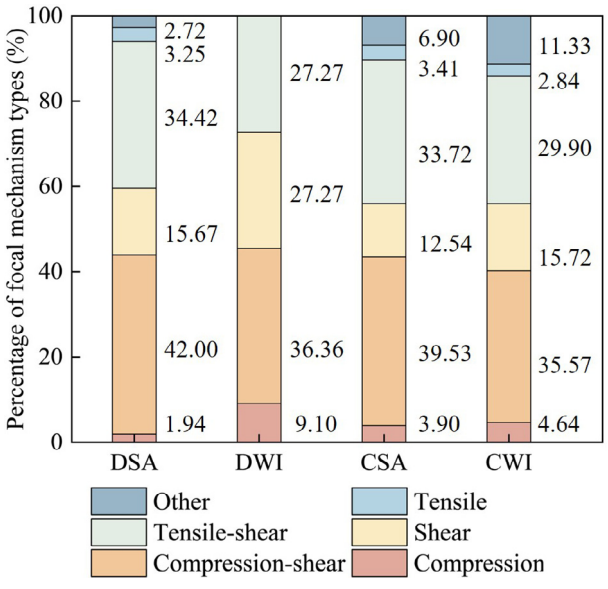

Fig. 16. Source types of AE events for different samples and stages.

(Fig. 18c), not only does the effective stress decrease (Circle A moves to Circle B), but the strength envelope also drops from the initial state to the unstable state. The synergy of the reduced effective normal stress and lowered frictional resistance promotes fault slip, causing the slip rate to increase continuously.

(2) Slip deceleration stage (Stage B to C): When the injection rate reaches a certain critical level (point C), the fluid causes an extremely high-water pressure gradient and severe strain heterogeneity near the injection hole. As shown in Fig. 18a, this extreme heterogeneity triggers secondary fracturing and rock crushing at the fault interface [41], which subsequently increases the geometric roughness of the fault, leading to a sharp increase in the friction coefficient. Therefore, although the effective stress continues to drop (Circle B moves to Circle C), the failure envelope shifts drastically upward to the fault rupture state. This enhanced anti-slip resistance dominates the system, thereby suppressing fault slip and causing the slip rate to decline.

Meanwhile, based on the Rate-and-State Friction (RSF) theory [42], the state of fault slip is primarily governed by the critical fault stiffness k_{crit}:

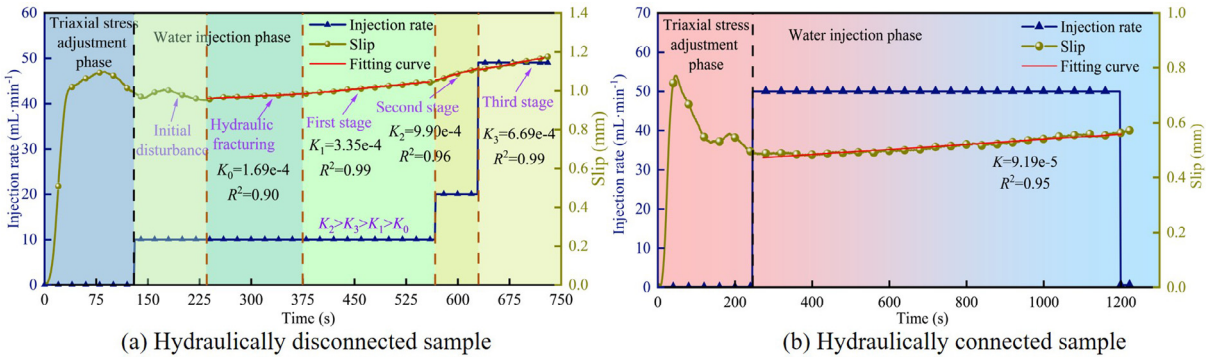

Fig. 17. Relationship between fault slip and fluid injection rate.

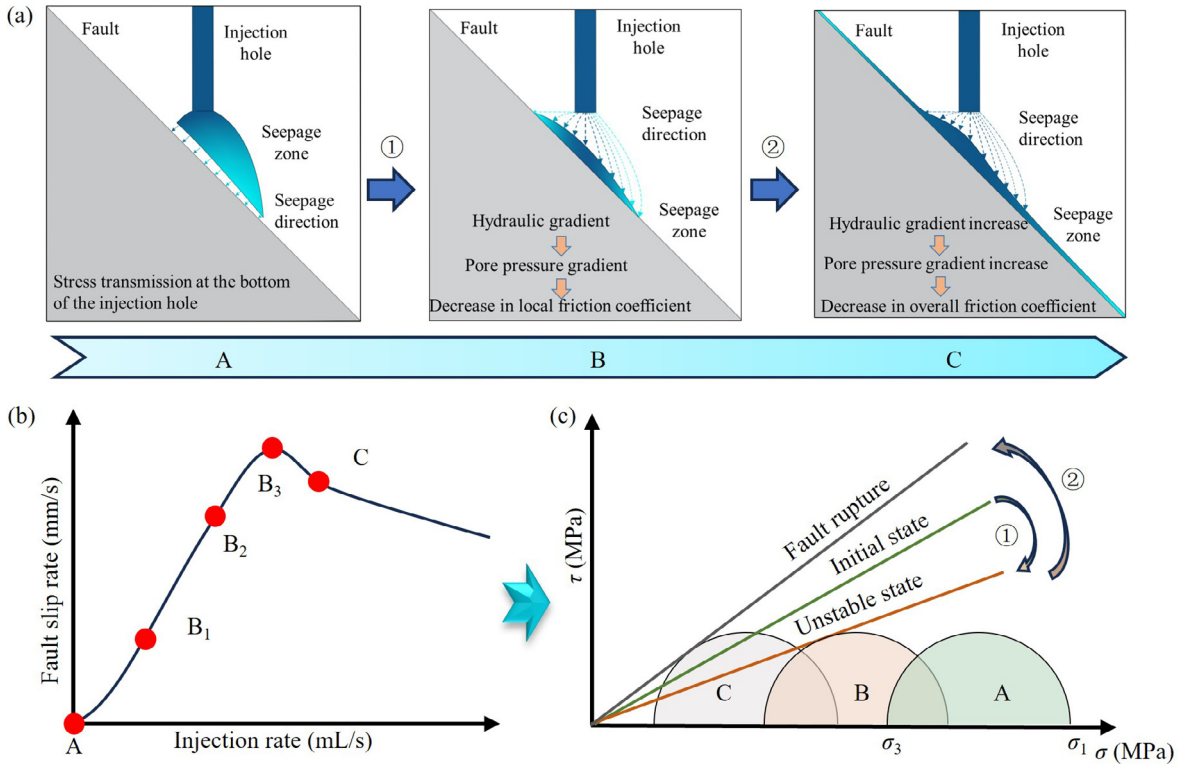

Fig. 18. Schematic diagram of the physical mechanisms underlying the non-linear relationship between fault slip rate and fluid injection rate.

$$k_{\text{crit}} = \frac{\sigma_n(b-a)}{D_c} \tag{11}$$

where σ_n is the effective normal stress; D_c the characteristic fault slip distance; and $(b–a)$ the fitting coefficient.

According to the Eq. (11), under the connected condition, a high injection rate leads to a steep surge in fault pore pressure and an instantaneous, drastic drop in σ_n. This subsequently causes a sudden plunge in the critical stiffness k_{crit}, ultimately triggering the release of a massive amount of elastic energy and dynamic rupture at the fault. Macroscopically, this is manifested by the generation of abundant AE events (Fig. 9b). Conversely, under the disconnected condition, the presence of low-permeability surrounding rock between the injection borehole and the fault causes the pore pressure at the fault to accumulate slowly, leading to a gradual decrease in σ_n. This provides the fault with sufficient time for stress redistribution and self-adjustment, allowing it to release energy slowly, which is manifested by the occurrence of only a few AE events (Fig. 8b).

4. Discussion

4.1. Faulted rock system state model

According to prior research [43], human activities such as underground mining, excavation, and fluid injection for hydraulic fracturing or pressure relief can alter the magnitude and direction of stresses within a faulted rock system, thereby impacting its overall stability. Therefore, accurate assessment of the stress state of this system requires accounting for changes in both stress magnitude and direction. It is worth noting that instability within a faulted rock system is not always derived from fault reactivation alone [44,45] Following the Mohr-Coulomb strength criterion, the fault is considered as a pre-existing weak plane. If the principal stress magnitudes remain constant but the principal stress directions rotate, failure may occur along weak planes within the surrounding rock mass. These weak planes could be the fault itself or other fractures

with different orientations. Consequently, assuming constant principal stress magnitudes, the faulted rock system can be categorised into 6 states (Fig. 19), corresponding to the possible combinations of principal stress rotations and their influence on potential failure planes.

(1) Stable state with no damage (Fig. 19a): The applied stress field is insufficient to cause damage to the fault or any weak plane in the surrounding rock.
(2) Weak plane failure without fault instability (Fig. 19b): When the mechanical strength of the weak plane in the surrounding rock is lower than that of the fault, the weak surface fails first under the applied stress. Although this failure redistributes stress around the fault, the redistributed stress remains insufficient to induce fault instability.
(3) Fault slip without weak-surface failure (Fig. 19c): When the weak plane in the surrounding rock is stronger than the fault, the fault becomes unstable first. This instability leads to stress redistribution, but the redistributed stress does not reach the strength threshold required to induce failure of the weak plane.
(4) Fault and weak surface coincide (Fig. 19d): When the fault coincides with the weak plane in the surrounding rock, instability of the fault produces shear failure along the weak plane.
(5) Fault slip followed by weak surface failure (Fig. 19e): When the weak plane in the surrounding rock is mechanically stronger than the fault, initial fault instability causes local stress redistribution. The increased stress near the weak plane subsequently results in its failure.
(6) Weak-surface failure followed by fault instability (Fig. 19f): When the weak plane in the surrounding rock is weaker than the fault, it fails first under the applied stress. The resulting stress redistribution near the fault then results in fault instability.

The stability of the faulted rock system is governed by the fault friction coefficient (μ), fault cohesion (c_f), the mechanical properties of the weak plane in the surrounding rock, and the ambient stress field. A mechanical model of the fault element is shown in Fig. 20, where the normal stress (σ_n) and shear stress (τ) acting on the fault plane are expressed as follows:

$$\sigma_n = \frac{\sigma_1 + \sigma_3}{2} + \frac{\sigma_1 - \sigma_3}{2}\cos 2\theta \tag{12}$$

$$\tau = \frac{\sigma_1 - \sigma_3}{2}\sin 2\theta \tag{13}$$

When the principal stress rotates by an angle δ,

$$\sigma_n = \frac{\sigma_1 + \sigma_3}{2} + \frac{\sigma_1 - \sigma_3}{2}\cos(2\theta + 2\delta) \tag{14}$$

$$\tau = \frac{\sigma_1 - \sigma_3}{2}\sin(2\theta + 2\delta) \tag{15}$$

According to the Mohr-Coulomb criterion, the ultimate shear strength of the fault can be expressed by:

$$\tau = \mu \cdot \sigma_n + c_f \tag{16}$$

Substituting Eqs. (14) and (15) into Eq. (16) yields the criterion of fault reactivation and slip under changes in the principal stress direction:

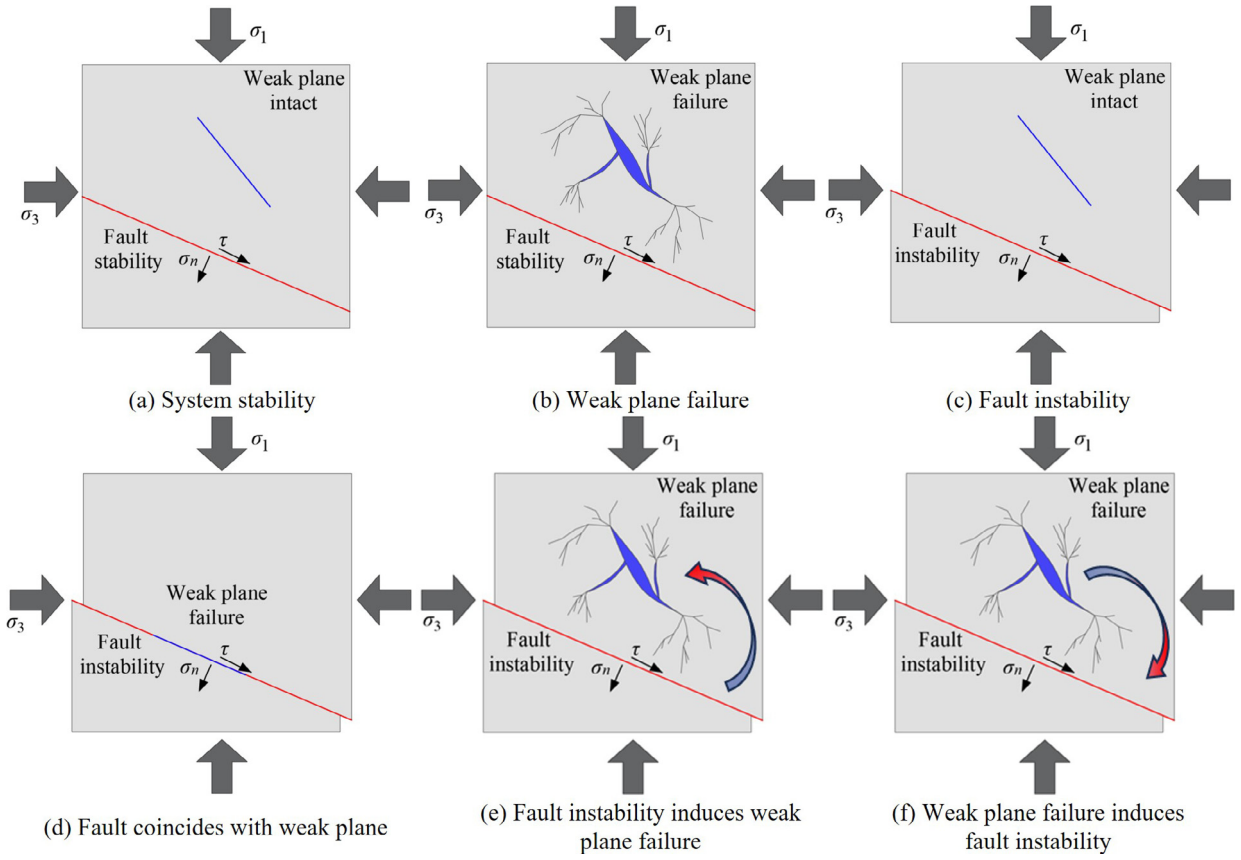

Fig. 19. Conceptual diagram of the fault-surrounding rock system states.

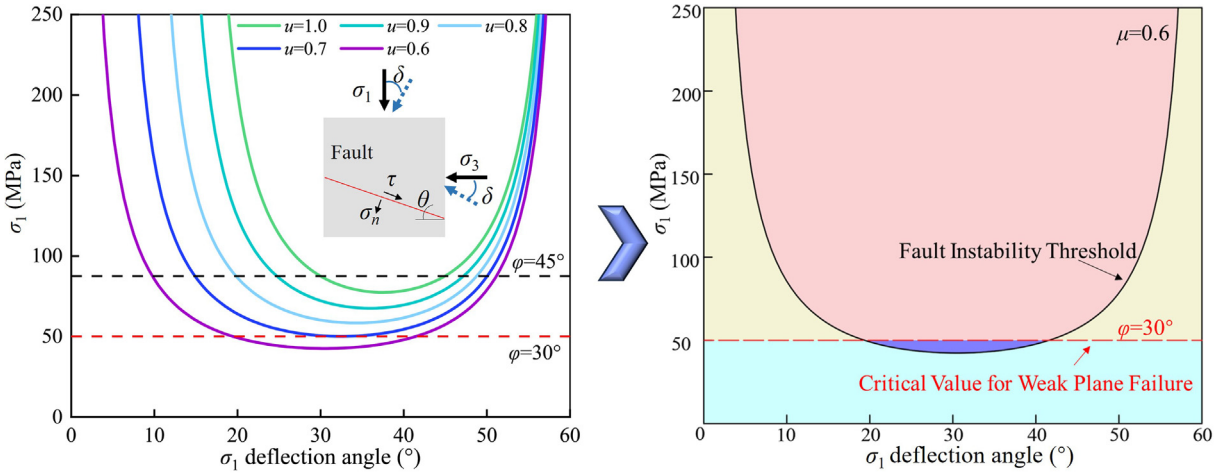

Fig. 20. Relationship of fault state with the deflection with respect to σ_1.

$$\sigma_{1\text{ - fault}} = \frac{2(c_f + \mu \cdot \sigma_3)}{[1 - \mu \cdot \cot(\theta + \delta)]\sin(2\theta + 2\delta)} + \sigma_3 \tag{17}$$

Eq. (17) shows a positive correlation between the critical state of fault reactivation and the parameters c_f, μ, and σ_3. Assuming a fault inclination angle θ=30°, c_f=6 MPa, and σ_3=10 MPa, the relationship between fault reactivation and the deflection angle δ can be examined with respect to σ_1.

The critical stress ($\sigma_{1\text{-rock}}$) required for the failure of this weak surface is determined in accordance with the Mohr strength criterion:

$$\sigma_{1\text{ - rock}} = 2c_r\sqrt{\frac{1+\sin\varphi}{1-\sin\varphi}} + \frac{1+\sin\varphi}{1-\sin\varphi}\sigma_3 \tag{18}$$

where c_r is the cohesion of the surrounding rock; and φ the internal friction angle of the surrounding rock.

Given that the surrounding rock and the fault exist within the same system, and assuming c_r=6 MPa, the critical stress ($\sigma_{1\text{-rock}}$) for the weak plane failure of the surrounding rock can be determined under the conditions of φ=30° and φ=45°. The dotted line represents the magnitude of $\sigma_{1\text{-rock}}$ required for the rock failure at different internal friction angles (φ). The resulting scenario is depicted in Fig. 20.

Fig. 20b illustrates a scenario with μ=0.6. In the stress environment represented by the green region, corresponding to Fig. 19a, the fault is stable. In contrast, the yellow, blue, and red regions correspond to Fig. 19b, c, e and f) respectively, representing instability when the fault acts as a weak plane within the surrounding rock. Thus, the green area denotes stability, whereas the yellow, blue, and red areas indicate instability.

Fig. 20a illustrates that as the mechanical strength (internal friction angle) of the surrounding rock increases, the proportion of the blue area increases while the yellow area decreases, indicating an initial increase in the probability of fault instability. Conversely, as μ rises, the blue area decreases, and the yellow area increases, suggesting a higher likelihood of the weak plane failing first. Therefore, adjusting fluid injection parameters during injection-induced fault slip is crucial, taking into account the mechanical strength of the fault and the surrounding rock under specific engineering conditions. In mining applications aimed at preventing fault-type rock bursts, it is essential to confine the stress field of the faulted rock system within the red and blue areas in Fig. 20b to promote fault slip and control energy release. In contrast, for geothermal systems, CO_2 storage, or natural gas extraction, optimal stress field control lies within the yellow area in Fig. 20b.

The conducted experimental tests involved hydraulically disconnected samples, as depicted in Fig. 19e, and hydraulically connected samples, as shown in Fig. 19d. Stress inversion was conducted to analyse the stress field distribution during the experiment, based on the AE events source mechanism at each stage. The three principal stress parameters considered for each AE event are the maximum principal stress σ_{1inv}, the intermediate principal stress σ_{2inv}, and the minimum principal stress σ_{3inv}. Normalisation was carried out following the proportional relationship among these principal stresses [46]:

$$R = \frac{\sigma_{1inv} - \sigma_{2inv}}{\sigma_{1inv} - \sigma_{3inv}} \tag{19}$$

where R is the shape ratio among the three principal stresses. A larger R value indicates that σ_{2inv} approaches σ_{3inv}. When R=1, the stress field is in an axisymmetric uniaxial compression state. When R=0, the stress field is in an axisymmetric biaxial compression state. When R=0.5, the stress field represents a relatively stable state.

For the normal stress σ_n and shear stress τ on the fault [47]:

$$\sigma_n = T_{0i}n_i = \tau_{ij}n_i n_j \tag{20}$$

$$\tau N_i = T_{0i} - \sigma_n n_i = \tau_{ij}n_j - \tau_{jk}n_j n_k n_i = \tau_{ik}n_j(\delta_{ik} - n_i n_k) \tag{21}$$

where δ_{jk} is the Kronecker delta; T_0 the dynamic force along the fault; n the normal direction of fault, and N the unit vector of shear stress acting on the fault.

For the calculation in Eq. (21), the Wallace-Bott assumption [48] was employed. The shear stress direction on the fault is assumed to align with the fault slip direction s, and tractive forces across different sections are considered constant. Upon normalising the shear stress on the fault, Eq. (21) can be reformulated as:

$$At = s \tag{22}$$

where t is the stress tensor satisfying σ_1+σ_2+σ_3=0, expressed as $t = [\tau_{11}\ \tau_{12}\ \tau_{13}\ \tau_{22}\ \tau_{23}]^T$.

The coefficient matrix A is a 3×5 matrix:

$$A = \begin{bmatrix} n_1(n_2^2+2n_3^2) & n_2(-n_1^2+n_3^2) & n_3(-2n_1^2-n_2^2) \\ n_2(1-2n_1^2) & n_1(1-2n_2^2) & -2n_1n_2n_3 \\ n_3(1-2n_1^2) & -2n_1n_2n_3 & n_1(1-2n_3^2) \\ n_1(-n_2^2+n_3^2) & n_2(n_1^2+2n_3^2) & n_3(-n_1^2-2n_2^2) \\ -2n_1n_2n_3 & n_3(1-2n_2^2) & n_2(1-2n_3^2) \end{bmatrix} \tag{23}$$

For the focal mechanisms of multiple AE events, a generalised linear inversion using the L2 norm can be applied to obtain:

$$t = A^{-g}s \tag{24}$$

In this work, the stress field inversion grid was divided according to the segmented spatio-temporal distribution of AE activity. Stress inversion was conducted at different stages for the two sample types used in this experiment. For each stage, 100 inversions were performed with random errors to assess the uncertainty in the stress inversion results. Fig. 21 depicts the distribution of principal stress directions, with red dots for σ_{1inv}, green dots for σ_2, and blue dots for σ_3. Fig. 22 illustrates the distribution of principal stress shape ratio R values at various stages.

During the stress adjustment stage, the principal stress distribution of both disconnected and connected samples is similar. For the disconnected sample, the azimuth angle of σ_{1inv} is 257.8°, with a plunge angle of 16.3°. In contrast, the azimuth angle of σ_{3inv} is 32.6°, with a plunge angle of 67.4°. The optimal fault solution shows a direction of 146.0° and a plunge of 42.5°, which closely aligns with the actual fault orientation, yielding R=0.709. For the connected sample, σ_{1inv} has an azimuth angle of 257.9°, with a plunge angle of 21.5°. In contrast, σ_{3inv} has an azimuth angle of 67.7° and a plunge angle of 68.2°. The optimal solution for the fracture plane is 163.0°, with a plunge angle of 44.9°, yielding R=0.611. This similarity arises because the loading stress ratios are consistent across samples, and the connectivity of the fluid injection hole has a minor influence on the overall stress direction. Furthermore, analysis of the stress shape ratio indicates that, during the stress adjustment stage, the faulted rock system exists in an axisymmetric uniaxial compression state dominated by σ_{1inv}.

During the fluid injection disturbance stage, for the disconnected sample, σ_{1inv} has an azimuth angle of 210.8° and a plunge angle of 14.8°, while σ_{3inv} has an azimuth angle of 10.0° and a plunge angle of 74.2°, yielding R=0.407. For the connected sample, σ_{1inv} has an azimuth angle of 138.8° and a plunge angle of 2.4°, while σ_{3inv} has an azimuth angle of 42.4° and a plunge angle of 69.2°, giving R=0.363. These findings suggest that during the fluid injection disturbance stage, the faulted rock system is in an axisymmetric biaxial compression state.

During the axisymmetric biaxial compression state, the significant lateral confinement provided by the high σ_2 effectively suppresses tensile failure. In contrast, during the axisymmetric uniaxial compression state, the insufficient constraint from σ_{2inv} facilitates the development of tensile fracturing within the rock mass. Consequently, as the stress state transitions from the stress adjustment stage to the fluid injection disturbance stage (Fig. 16), the proportions of compressive-shear and tensile-shear focal mechanisms decrease, whereas the proportion of pure shear focal mechanisms increases.

By comparing the changes in the stress field across different samples during the two stages, it becomes evident that the stress state of the faulted rock system evolves throughout the fluid injection process. Notably, variations in the azimuth angle of the stress field primarily govern the direction of fault slip, while changes in the inclination angle significantly influence the fault stability. For instance, in the connected specimen, the angle between the maximum principal stress σ_{1inv} and the fault plane during the stress adjustment phase is significantly smaller than that during the fluid injection perturbation phase. Meanwhile, as illustrated in Fig. 23, the local stress shape ratio (R-value), inverted from AE focal mechanisms, does not reach stability immediately upon water injection. Instead, it exhibits intense dynamic fluctuations with increasing injection time before gradually converging toward a stable range. This dynamic adjustment process intuitively demonstrates that fluid-induced fault instability is not solely governed by a simple reduction in effective normal stress; the dynamic redistribution and rotation of the local three-dimensional stress field (the shape of the stress tensor) also plays a crucial driving role. It is worth noting that, due to the inherent limitations of current AE inversion techniques, this experiment can only invert the relative shape of the local stress field (R-value) and the directions of the principal stress axes, but cannot yet provide the absolute dynamic magnitudes of each principal stress. This limitation will be addressed in future research.

4.2. Influence of permeability of the faulted rock system

In practical engineering scenarios, rock with varying permeability influences the formation of the fracture network during hydraulic fracturing, thereby influencing the impact of fluid flow on fault slip. This phenomenon can be categorised into six scenarios and four types, as illustrated in Fig. 24.

(1) High-permeability rock with an injection well connected to the fault (Fig. 24a): Fluid injection increases pore pressure in both the rock and the fault, promoting fault reactivation. If the fault has high permeability, reactivation is more likely. Conversely, low-permeability faults resist water penetration, making reactivation difficult and potentially generating new fracture surfaces within the rock.
(2) High-permeability rock with an injection well disconnected from the fault (Fig. 24b and c): Water permeates to the rock towards the fault, raising pore pressure within the fault and inducing fault reactivation. The subsequent fault slips response follows the same process described in Scenario 1.

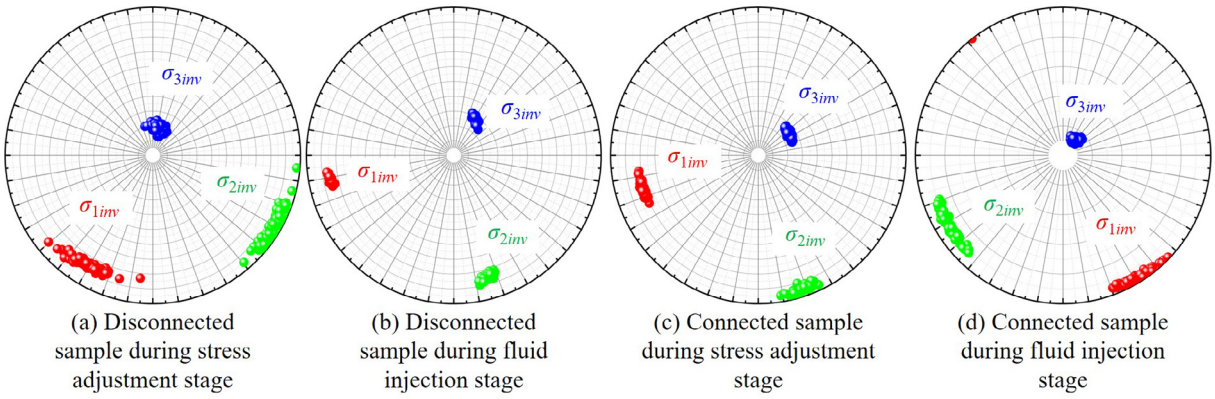

Fig. 21. Distribution of principal stresses for different samples and stages.

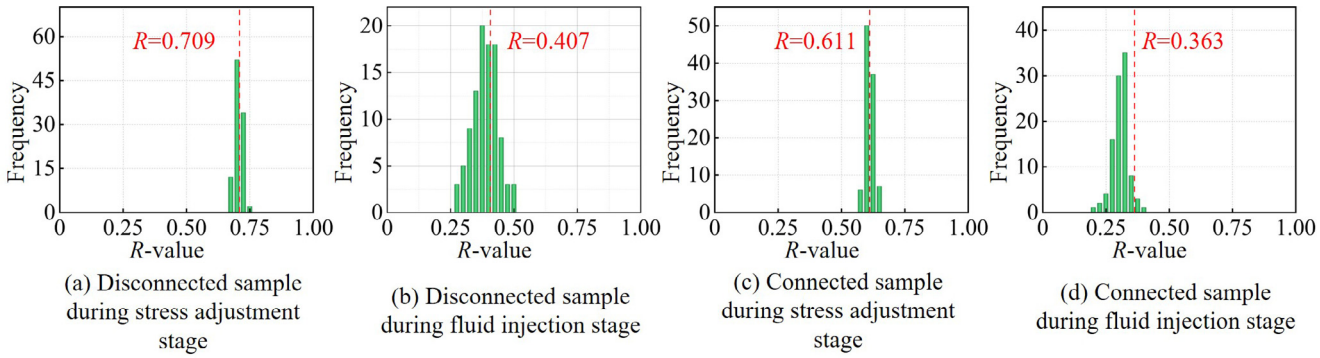

Fig. 22. Distribution of the main stress shape ratio *R* value for different samples and stages.

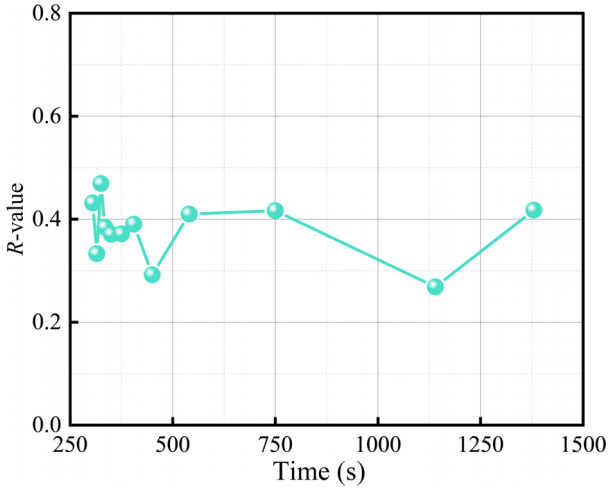

Fig. 23. Dynamic evolution of the *R*-value during the fluid injection stage in the connected specimen.

(3) Low-permeability rock with an injection well disconnected from the fault (Fig. 24d): Increasing pore pressure within the rock is challenging. Fluid injection primarily raises pore pressure within the fault, which can lead to fault reactivation. High-permeability faults are more susceptible to reactivation, whereas low-permeability faults require higher fluid injection pressures [49].
(4) Low-permeability rock with an injection well disconnected from the fault (Fig. 24e and f): High-pressure hydraulic fracturing is necessary to influence the fault within the rock. This increases the pore pressure at the fault or generates poroelastic stress, thereby inducing fault reactivation. A notable lag exists between hydraulic fracturing and fault reactivation, but the overall process aligns with Scenario 3.

Fig. 3a illustrates that the yellow sandstone used in this study is low-permeability, while the absence of fault mud indicates the presence of a high-permeability fracture. Consequently, the hydraulically disconnected samples align with the scenario depicted in Fig. 24e, while the connected samples correspond to the scenario shown in Fig. 24d. Analysis of Figs. 14b and 15b shows that fault slip in the disconnected sample is predominantly aseismic slip, whereas seismic slip occurs in the connected sample.

From the perspective of preventing and controlling fault-type rock bursts in mining areas, a significant number of AE events occur during fluid injection in the hydraulically connected sample, thereby releasing energy from the faulted rock system. Regarding the stress field, fluid injection has a more pronounced effect on the direction of σ_{1inv} in the connected sample than in the disconnected sample. Therefore, for low-permeability rock strata, establishing a connection between the fault with the injection hole is more effective in preventing uncontrolled failure.

5. Conclusions

This work investigates two working conditions of subsurface fluid injection: fluid injection holes either connected or disconnected from the fault. Experiments were conducted on fault slip induced by varying fluid injection conditions under true triaxial stress with varying injection rates. The study explores the mechanisms driving fluid injection-induced fault slip and the associated seismic response. The main conclusions are as follows:

(1) The fault slip induced by fluid injection occurs in three stages: fluid injection disturbance, hydraulic fracturing, and pore pressure increase within the fault. The spatio-temporal distribution and spectral analysis of AE events during the disturbance and fracturing stages indicate that the mechanical mechanism governing fault slip is predominantly influenced by poroelastic coupling.
(2) Fluid injection-induced fault slip and fracture development are interdependent. The development of fractures increases the pore pressure within the fault, altering the state of fault slip. Conversely, fault slip alleviates local pressure, which in turn promotes further fracture development.
(3) Seismic responses of hydraulic fracturing and fault slip under true triaxial stress conditions exhibit distinct characteristics. Fault slip originates primarily from compressive-shear sources, whereas hydraulic fracturing is associated with tensile-shear sources.
(4) The fluid injection rate effectively controls the fault slip state. In low-permeability surrounding rocks, direct fluid injection through faults is more effective in regulating fault slip. In contrast, in high-permeability strata, hydraulic fracturing near the fault is more efficient.
(5) A mechanical model of the faulted rock system was established based on rock strength and stress field evolution. As the mechanical strength of the rock increases, the likelihood of fault instability preceding rock failure also increases. Reasonable control ranges for different working conditions were also identified.

CRediT authorship contribution statement

Linzhi Wang: Writing – original draft, Data curation, Conceptualization. **Wu Cai:** Supervision, Project administration, Funding

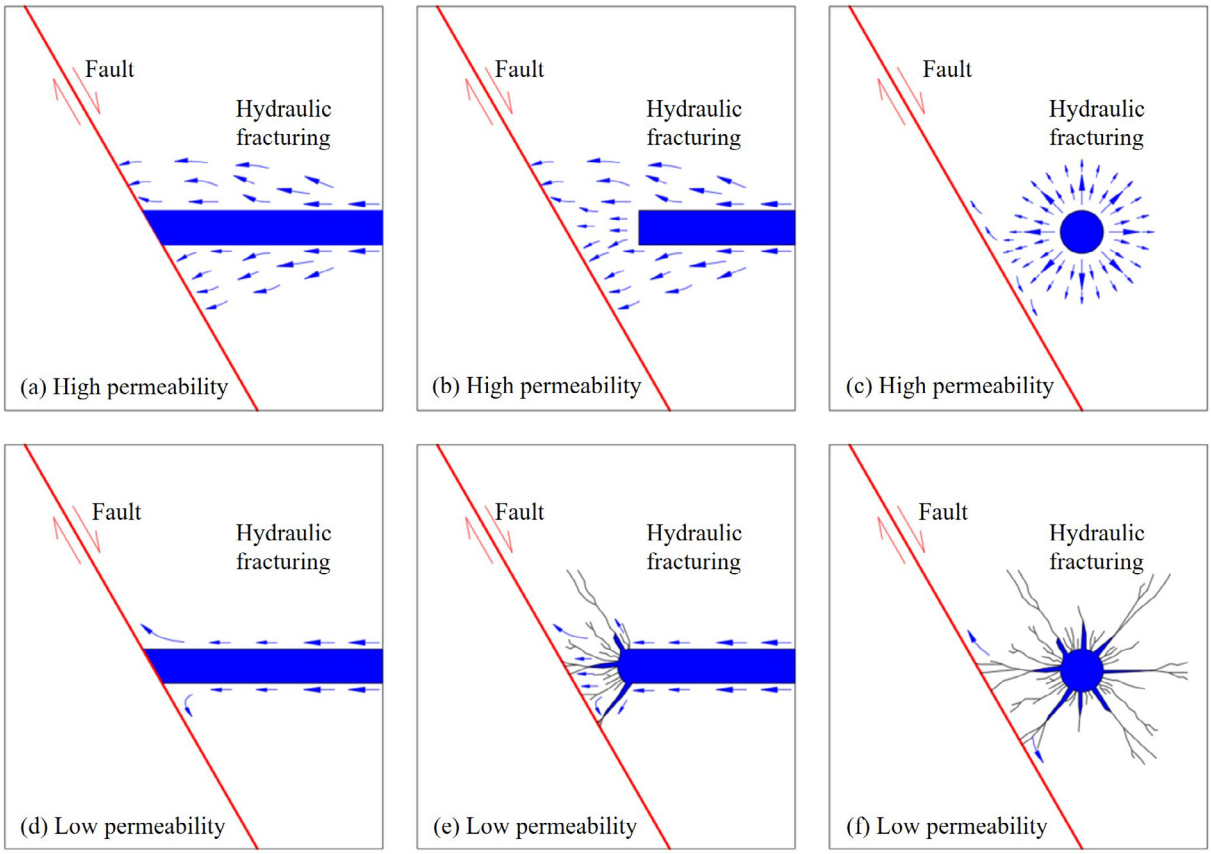

Fig. 24. Diagram illustrating the activation process of faults induced by hydraulic fracturing.

acquisition. **Wenzhuo Cao:** Writing – review & editing. **Lee J. Hosking:** Writing – review & editing. **Ruijia Wang:** Writing – review & editing. **Mehdi Zare:** Writing – review & editing.

Declaration of competing interest

The authors declare that they have no known competing financial interests or personal relationships that could have appeared to influence the work reported in this paper.

Acknowledgments

This work was supported by the Program of National Natural Science Foundation of China (Nos. 52374101, 32111530138 and W2421032), the Jiangsu Province International Collaboration Program-Key National Industrial Technology Research and Development Cooperation Project (No. BZ2024024), and the Independent Research Project of State Key Laboratory for Fine Exploration and Intelligent Development of Coal Resources, CUMT (No. SKLCRSM24X005).

References

[1] Ratouis TMP, Snæbjörnsdóttir SÓ, Voigt; MJ, Sigfússon B, Gunnarsson G, Aradóttir ES, et al. Carbfix 2: a transport model of long-term CO_2 and H_2S injection into basaltic rocks at Hellisheidi. SW-Iceland Int J Greenh Gas Control 2022;114:103586.
[2] Montgomery-Brown EK, Shelly DR, Hsieh PA. Snowmelt-triggered earthquake swarms at the margin of long valley caldera. California Geophys Res Lett 2019;46(7):3698–705.
[3] Wilson MP, Foulger GR, Gluyas JG, Davies RJ, Julian BR. HiQuake: the human-induced earthquake database. Seismol Res Lett 2017;88(6):1560–5.
[4] Zhuang JX, Mu ZL, Cai W, He H, Lee JH, Xi GJ, et al. Multistage hydraulic fracturing of a horizontal well for hard roof related coal burst control: insights from numerical modelling to field application. Int J Min Sci Technol 2024;34(8):1095–114.
[5] Ju Y, Fu GM, Zhou HW, Ge SR, Peng SP. Fault reactivation and seismic risks induced by deep reservoir fracturing: mechanisms, prediction and perspectives. Int J Min Sci Technol 2025;35(8):1211–32.
[6] Healy JH, Rubey WW, Griggs DT, Raleigh CB. The Denver earthquakes. Science 1968;161(3848):1301–10.
[7] Elsworth D, Spiers CJ, Niemeijer AR. Understanding induced seismicity. Science 2016;354(6318):1380–1.
[8] Raleigh CB, Healy JH, Bredehoeft JD. An experiment in earthquake control at Rangely. Colorado Science 1976;191(4233):1230–7.
[9] Ling FL, Duan K, Shang JL. Hydro-mechanical behavior of mineralized faults in granite during fluid injection: insights from triaxial shear-flow experiments. Eng Geol 2026;361:108499.
[10] Huang YM, Ma SL, Li XH. Research progress on injection-induced earthquakes. J Earthq Eng 2023;45(2):387–400. in Chinese.
[11] Grigoli F, Cesca S, Priolo E, Rinaldi AP, Clinton JF, Stabile TA, et al. Current challenges in monitoring, discrimination, and management of induced seismicity related to underground industrial activities: a European perspective. Rev Geophys 2017;55(2):310–40.
[12] Hainzl S, Ogata Y. Detecting fluid signals in seismicity data through statistical earthquake modeling. J Geophys Res 2005;110(B5).
[13] Liang X, Xu TF, Chen JY, Jiang ZJ. A deep-learning based model for fracture network characterization constrained by induced micro-seismicity and tracer test data in enhanced geothermal system. Renew Energy 2023;216:119046.
[14] House L, Phillips WS, Fehler M, Rutledge J. Can hydraulic fracture-induced microearthquakes show where the fluid went? Int J Rock Mech Min Sci 1997;34(3–4):133.e1–133.e15.
[15] Orlecka-Sikora B, Cielesta S, Lasocki S. Tracking the development of seismic fracture network from the Geysers geothermal field. Acta Geophys 2019;67(1):341–50.
[16] Zhang HL, Eaton DW, Li G, Liu YJ, Harrington RM. Discriminating induced seismicity from natural earthquakes using moment tensors and source spectra. JGR Solid Earth 2016;121(2):972–93.
[17] Zhao Y, Yang TH, Zhang PH, Xu HY, Wang SH. Inversion of seepage channels based on mining-induced microseismic data. Int J Rock Mech Min Sci 2020;126:104180.

[18] Yan X, Yu HT, Jing HW. Numerical investigation of the stress regime effect on injection-induced fault reactivation and associated seismicity. Comput Geotech 2024;169:106251.
[19] Wang L, Kwiatek G, Renard F, Guérin-Marthe S, Rybacki E, Bohnhoff M, et al. Fault roughness controls injection-induced seismicity. PNAS 2024;121(3):e2310039121.
[20] Lv YX, Yuan C, Zhu XH, Gan Q, Li HB. THMD analysis of fluid injection-induced fault reactivation and slip in EGS. Geothermics 2022;99:102303.
[21] Cao WZ, Shi JQ, Si GY, Durucan S, Korre A. Numerical modelling of microseismicity associated with longwall coal mining. Int J Coal Geol 2018;193:30–45.
[22] Oye V, Stanchits S, Cerasi P, Seprodi N, Goertz-Allmann B, Bauer RA. Understanding the causes of fluid-induced seismicity through large-block ~1 m^3 laboratory experiments. 14th GHGT-14 Melbourne 2018;10:21–6.
[23] Rodríguez-Pradilla G, Eaton DW, Verdon JP. Basin-scale multi-decadal analysis of hydraulic fracturing and seismicity in western Canada shows non-recurrence of induced runaway fault rupture. Sci Rep 2022;12:14463.
[24] Cao WZ, Zhang R, Nie XF, Ren L. Laboratory fracture slip and seismicity subjected to fluid injection-related stress and pressure paths. Rock Mech Rock Eng 2024;57(2):1245–61.
[25] Cao WZ, Yildirim B, Durucan S, Wolf KH, Cai W, Agrawal H, et al. Fracture behaviour and seismic response of naturally fractured coal subjected to true triaxial stresses and hydraulic fracturing. Fuel 2021;288:119618.
[26] Huang YH, De Barros L, Cappa F. Illuminating the rupturing of microseismic sources in an injection-induced earthquake experiment. Geophys Res Lett 2019;46(16):9563–72.
[27] Guglielmi Y, Cappa F, Avouac JP, Henry P, Elsworth D. Seismicity triggered by fluid injection-induced aseismic slip. Science 2015;348(6240):1224–6.
[28] Wang L, Kwiatek G, Rybacki E, Bonnelye A, Bohnhoff M, Dresen G. Laboratory study on fluid-induced fault slip behavior: the role of fluid pressurization rate. Geophys Res Lett 2020;47(6).
[29] Gori M, Rubino V, Rosakis AJ, Lapusta N. Dynamic rupture initiation and propagation in a fluid-injection laboratory setup with diagnostics across multiple temporal scales. PNAS 2021;118(51):e2023433118.
[30] Aben FM, Farsi A, Brantut N. Permeability development during fault growth and slip in granite. JGR Solid Earth 2024;129(12).
[31] Zhang X, Si GY, Oh J, Zhao GZ. Evolution of crack source mechanisms in laboratory hydraulic fracturing on Harcourt granite. Rock Mech Rock Eng 2024;57(10):7945–61.
[32] Zhang HW, Wan ZJ, Zhao YX, Zhang Y, Lu SF. A review of the research on the mechanism of hydro-shearing in geothermal reservoir. J Coal Soc 2021;46(10):3172–85. in Chinese.
[33] Liu B, Geng Z, Kang YS, Liu XW, Zhou Y, Liu QS, et al. Fault slip behaviors and frictional stability controlled by particle size of fault gouge under fluid injection. Int J Rock Mech Min Sci 2024;183:105919.
[34] Cai W, Dou LM, Si GY, Hu YW. Fault-induced coal burst mechanism under mining-induced static and dynamic stresses. Engineering 2021;7(5):687–700.
[35] Wang TA, Dunham EM. Hindcasting injection-induced aseismic slip and microseismicity at the Cooper Basin enhanced geothermal systems project. Sci Rep 2022;12:19481.
[36] Lapins S, Roman DC, Rougier J, De Angelis S, Cashman KV, Kendall JM. An examination of the continuous wavelet transform for volcano-seismic spectral analysis. J Volcanol Geoth Res 2020;389:106728.
[37] Das I, Long-period ZMD. long-duration seismic events during hydraulic stimulation of shale and tight-gas reservoirs. Part 1: Waveform characteristics. Geophysics 2013;78(6):KS107–18.
[38] Peng ZG, Gomberg J. An integrated perspective of the continuum between earthquakes and slow-slip phenomena. Nature Geosci 2010;3(9):599–607.
[39] Wang L, Kwiatek G, Bohnhoff M, Rybacki E, Dresen G. Injection-induced fault slip and associated seismicity in the lab: insights from source mechanisms, local stress states and fault geometry. Earth Planet Sci Lett 2024;626:118515.
[40] Hudson JA, Pearce RG, Rogers RM. Source type plot for inversion of the moment tensor. J Geophys Res 1989;94(B1):765–74.
[41] Fu PC, Schoenball M, Ajo-Franklin JB, Chai CP, Maceira M, Morris JP, et al. Close observation of hydraulic fracturing at EGS Collab Experiment 1: fracture trajectory, microseismic interpretations, and the role of natural fractures. JGR Solid Earth 2021;126(7).
[42] Zhu AY, Sun ZH, Jiang CS, Chen S, Zhang DN, Cui GL. The dynamic mechanical response of the fault under different water injection schedules. Acta Seismol Sin 2021;43(6):730–44. in Chinese.
[43] Li J, Zhang R, Yu Y, Yu JD, Xie PS, Lang D. Risk assessment of roof fault activation induced by mining stress deflection in mining roadway. J Rock Mech Eng 2023;42(S2):4109–20. in Chinese.
[44] Wei T, Chen GQ, Zhu Z, Tang P, Yan M. Slope instability mechanism with differential rock mass structure along a fault: a mine landslide from Southwest China. Geomech Geophys Geo Energy Geo Resour 2024;10(1):76.
[45] Zhang SP, Ji YL, Hofmann H, Li SD, Rybacki E, Zimmermann G, et al. A laboratory study on fault slip caused by fluid injection directly versus indirectly into a fault: implications for induced seismicity in EGSs. Phil Trans R Soc A 2024;382(2276):20230186.
[46] Vavryčuk V. Iterative joint inversion for stress and fault orientations from focal mechanisms. Geophys J Int 2014;199(1):69–77.
[47] Tang C, Li SL, Zhou MJ, Liu YC. Stress inversion based on microseismic monitoring and its engineering application. J Geotech Eng 2021;43(9):1730. in Chinese.
[48] Bott MHP. The mechanics of oblique slip faulting. Geol Mag 1959;96(2):109–17.
[49] Zhu JB, Kang JQ, Elsworth D, Xie HP, Ju Y, Zhao J. Controlling induced earthquake magnitude by cycled fluid injection. Geophys Res Lett 2021;48(19).